Mathematics

AIMS Mathematics, 11(8): 25470–25505.
DOI: 10.3934/math.20261022
Received: 14 June 2026
Revised: 31 July 2026
Accepted: 05 August 2026
Published: 18 August 2026

https://www.aimspress.com/journal/Math

Research article

A Riemannian manifold-valued trajectory modeling and elastic alignment framework: A cable degradation case study

Zigang Liu[1,2], Tianyao Ji[1,*], Zeineb Klai[3,*] and Saleh M. Altowaijri[4]

[1] School of Electric Power Engineering, South China University of Technology, Guangzhou 510641, China
[2] School of Electrical and Electronic Engineering, Nanyang Technological University, 639798, Singapore.
[3] Department of Computer Sciences, Faculty of Computing and Information Technology, Northern Border University, Rafha 91911, Saudi Arabia
[4] Department of Information Systems, Faculty of Computing and Information Technology, Northern Border University, Rafha 91911, Saudi Arabia

* **Correspondence:** Email: tyji@scut.edu.cn; Zeineb.klai@nbu.edu.sa.

Abstract: Cable degradation is a nonlinear evolution process affected by structural, thermal, and spatial factors, which may introduce complex distortions into measured cable responses. Conventional Euclidean indicators based on fixed points, empirical sub-bands, or direct vector distances are often insufficient to represent such coupled variations. To address this issue, this paper proposes a Riemannian manifold-valued trajectory modeling and elastic alignment framework for analyzing cable degradation. The measured cable responses are first converted into localized symmetric positive definite (SPD) covariance matrices using a sliding-window strategy, representing each cable state as a continuous trajectory on the SPD manifold. These trajectories are then elastically aligned using the proposed log-Euclidean dynamic time warping (LE-DTW) framework, yielding two geometric descriptors: A warping path for horizontal parameter distortion and a residual shape distance for intrinsic geometric variation. Based on the residual distance, cumulative Riemannian shape energy (CRSE) is constructed and normalized into a monotonic health index (HI) for retrospective within-trajectory analysis. A causal cumulative degradation feature, which does not require terminal failure information, is further combined with the warping energy for independent cross-temperature predictions of remaining useful life. In the retrospective analysis, the proposed HI + CRSE representation reduces root mean squared error (RMSE) from 23.4370% to 0.9404% and mean absolute error from 15.5850% to 0.6768%, while increasing R^2 from 0.3808 to 0.9990. In the independent cross-temperature experiment, Gaussian process regression models trained exclusively on the 160 ℃ trajectories are tested on independent 140 ℃ cables with lengths of 1 m, 2 m, and 3 m, obtaining RMSE values of 4.7237%, 5.5727%, and 1.8697%, respectively.

Keywords: Riemannian manifold; SPD matrix; manifold-valued trajectory; elastic alignment; dynamic time warping; geometric modeling; non-Euclidean representation cable degradation
Mathematics Subject Classification: 15B48; 53B21; 65D10; 68W40; 90C39

1. Introduction

Cable insulation degradation is one of the major threats to the safe and reliable operation of power transmission and distribution systems [1]. Modern power systems are increasingly affected by renewable energy fluctuations, operational uncertainty, and planning complexity, which further increases the demand for reliable equipment condition assessment and asset management [2–4]. Under long-term thermal, electrical, mechanical, and environmental stresses, cable insulation materials gradually experience changes in dielectric relaxation, increased conductivity, microstructural deterioration, local discontinuities, and eventually insulation failure [5,6]. Therefore, cable degradation analysis requires not only sensitive measurements but also a mathematical representation capable of describing the nonlinear evolution of the response under different structural, thermal, and spatial conditions.

Traditional cable insulation assessment methods include measurements of insulation's resistance or conductivity, measurement of dielectric loss, partial discharge detection, frequency-domain reflectometry (FDR), time-domain reflectometry (TDR), and broadband impedance-based analysis. Insulation resistance and low-conductivity measurements can reflect global insulation deterioration but they are usually less sensitive to early-stage or localized degradation [7]. Dielectric loss measurement, especially low-frequency tan δ, has been widely used for cable aging assessment, although it mainly provides an overall condition indicator [8]. Partial discharge diagnosis is effective for detecting voids and severe defects, but it may not respond clearly to nondischarge-type thermal aging [9]. Reflectometry-based methods can locate impedance discontinuities through reflected signals; FDR has been applied to aging wiring tests; and TDR has been used for cable defect detection and localization [10,11]. Broadband impedance responses provide richer information because polarization, conduction, resonance behavior, distributed parameters, and local degradation may all be reflected over a wide frequency range [12,13].

However, broadband cable responses are difficult to compare directly. The measured magnitude of impedance and phase angle are not only affected by the material's degradation, but also by cable length, distributed resistance–inductance–conductance–capacitance parameters, aging temperature, and aging location. These factors may introduce resonance shifts, frequency axis misalignment, local spectral distortions, and nonmonotonic fluctuations [12,13]. As a result, Euclidean indicators extracted from fixed frequencies, selected sub-bands, or vectorized spectra may confuse horizontal parameter axis distortion with intrinsic degradation-related shape changes. A large pointwise distance may therefore arise from a loss of correspondence rather than from a true change in the cable's state.

Data-driven degradation modeling methods, including principal component analysis, machine learning, health index construction, feature fusion, and uncertainty-aware remaining useful life (RUL) prediction, have been widely used for prognostics and health management [14–16]. These methods are useful for compressing high-dimensional measurements and mapping features to degradation labels. Nevertheless, they generally do not explicitly determine which samples should correspond when spectral structures move along the sampling axis. Fixed-frequency descriptors make the correspondence assumption implicit, while direct dimensionality reduction may preserve the dominant variance without separating parameter distortion from intrinsic geometric variation.

This difficulty can be regarded as a mathematical problem of comparing ordered multichannel curves. Dynamic time warping (DTW) provides a classical solution for monotone sequence alignment [17,18], but conventional DTW is usually performed on Euclidean samples and does not account for the local covariance geometry of multichannel observations. For cable responses, magnitude of impedance and phase are coupled within local frequency neighborhoods, and this second-order structure may be lost if the channels are compared independently or treated as ordinary vectors. Therefore, a suitable representation should preserve the local variance–covariance information, while a suitable alignment should allow nonlinear but order-preserving reparameterization of the sampling axis.

Riemannian geometry provides a natural framework for this purpose. A regularized local covariance matrix is symmetric positive definite (SPD) and thus lies on the SPD manifold rather than in an unconstrained Euclidean space. Matrix logarithms, geodesic distances, and invariant metrics provide a coherent calculus for SPD-valued data [19–25]. By sliding a covariance window along the ordered cable response, each measurement can be lifted into an SPD-valued trajectory, preserving both the local coupling between channels and the order of the sampling axis. This converts cable degradation analysis from fixed-feature extraction into manifold-valued trajectory modeling.

Beyond covariance-based signal analysis, Riemannian geometry has increasingly been applied to graph representation learning. Representative studies include hyperbolic graph convolutional networks [26], SPD-manifold graph networks [20], manifold-valued spiking graph neural networks [27], and Riemannian graph foundation models [28]. For knowledge graph completion, multiview Riemannian manifold fusion combines hyperbolic, Euclidean, and spherical spaces to capture complementary structures [29]. RiemannGL further summarizes these developments as a unified Riemannian graph-learning paradigm [30]. In contrast, this study focuses on the elastic alignment of ordered SPD-valued trajectories, jointly considering local covariance geometry and parameter axis correspondence.

The remaining issue is parameterization. Two SPD-valued trajectories may trace similar geometric patterns at different frequency locations because of resonance shifts, cable-length effects, or localized degradation. Elastic curve analysis treats such effects as changes in the traversal speed, allowing the intrinsic trajectory shape to be compared after reparameterization. In square root velocity function (SRVF) coordinates, the action of a monotone reparameterization has a norm-preserving form, which is suitable for separating parameter axis distortion from residual shape variation [31,32]. Combined with DTW-type dynamic programming [18,33], this leads to a log-Euclidean dynamic time warping (LE-DTW), which provides a practical discrete alignment strategy for sampled SPD-valued trajectories.

Motivated by these considerations, this paper proposes a Riemannian manifold-valued trajectory modeling and elastic alignment framework for analyzing cable degradation. The measured cable responses are first converted into sequences of localized SPD covariance matrices. The principal matrix logarithm is used to obtain log-Euclidean coordinates, and the resulting trajectories are presented in SRVF form. These trajectories are then aligned using LE-DTW to estimate the optimal monotone correspondence. The same optimization yields two complementary geometric quantities: An optimal warping path describing frequency axis deformation and a residual shape distance describing postalignment geometric variation. Based on the residual shape distance, the cumulative Riemannian shape energy (CRSE) is constructed and normalized into a monotonic health index (HI). The HI and warping energy are further fused and used in Gaussian process regression (GPR) for probabilistic RUL prediction.

The main contributions of this paper are summarized as follows.

(1) A local covariance lifting operator is developed to transform ordered cable responses into SPD-valued trajectories, preserving local variance–covariance coupling between the magnitude of impedance and phase.

(2) An LE-DTW-based elastic alignment strategy is formulated in log-Euclidean SRVF coordinates, enabling geometry-aware correspondence estimation for multivalued cable trajectories.

(3) The proposed alignment decomposes variations in the cable response into frequency axis warping and residual geometric shape discrepancies, providing an interpretable non-Euclidean description of the evolution of cable degradation.

(4) CRSE is constructed from the residual shape distance and normalized into a monotonic HI for retrospective interpretation of degradation and within-trajectory mapping. A causal cumulative feature is further developed and combined with the warping energy for independent cross-temperature RUL prediction without using target or terminal information from the evaluated cable.

2. Materials and methods

2.1. SPD representation and metric structure

In d-channel broadband impedance spectroscopy (BIS) analyses, the localized covariance matrices of impedance features naturally reside in the SPD manifold. The d-dimensional SPD manifold, denoted as $\mathcal{M} = \mathcal{S}_{++}^{d}$, is defined as

$$\mathcal{M} = \left\{ C \in \mathbb{R}^{d\times d} : C^{\mathrm{T}} = C, u^{\mathrm{T}} C u > 0, \forall u \in \mathbb{R}^{d} \backslash \{0_d\} \right\}. \tag{1}$$

Geometrically, $\mathcal{M}$ constitutes an open convex cone within the $d\left(d+1\right)/2$ dimensional vector space of symmetric matrices. Unlike Euclidean space, this manifold possesses nonzero Riemannian curvature.

2.2. Tangent spaces and logarithmic/exponential mappings

At any point $C \in \mathcal{M}$, its local linear approximation is defined as the tangent space $\mathcal{T}_C\mathcal{M} \cong \mathcal{S}ym(d)$, where $\mathcal{S}ym(d)$ is the space of real symmetric matrices. The mapping between the curved manifold $\mathcal{M}$ and the flat tangent space is governed by the logarithmic map ($\log_C$) and exponential map ($\exp_C$) [24].

For any matrix $C \in \mathcal{M}$, the spectral decomposition theorem guarantees that C can be factorized as

$$C = U \Lambda U^{\mathrm{T}}, \tag{2}$$

where $U \in \mathbb{R}^{d \times d}$ is the orthogonal eigenvector matrix satisfying $U^{\mathrm{T}} U = I_d$, and $\Lambda = \mathrm{diag}(\lambda_1, \lambda_2, \ldots, \lambda_d)$ is the diagonal eigenvalue matrix whose diagonal entries λ_i represent the i-th eigenvalue of C.

The matrix logarithm and exponential operators are explicitly computed as follows:

$$\log(C) = U \mathrm{diag}(\ln \lambda_i) U^{\mathrm{T}}, \tag{3}$$

$$\exp(C) = U \mathrm{diag}(e^{\lambda_i}) U^{\mathrm{T}}. \tag{4}$$

Under the log-Euclidean framework, mapping a manifold point $P \in \mathcal{M}$ to the reference tangent space at the identity matrix I simplifies significantly to

$$\log_I(P) = \log(P) \in \mathcal{S}ym(d), \tag{5}$$

$$\exp_I(V) = \exp(V) \in \mathcal{M}. \tag{6}$$

2.3. Geodesic curves and distance formulations

A geodesic curve $\eta(s):[0,1] \to \mathcal{S}_{++}^d$ represents the shortest path on the SPD manifold between two state configurations, where s is the normalized geodesic parameter. The length of this minimal curve defines the Riemannian distance function, which has been widely used to compare SPD matrices and covariance descriptors under non-Euclidean geometry [25].

2.3.1. Affine-invariant Riemannian metric (AIRM) geodesic and distance

Under the AIRM, the unique geodesic equation initializing at $\eta(0) = C_1$ and terminating at $\eta(1) = C_2$ takes the form of a geometric matrix power function

$$\eta_{\mathrm{AIRM}}(s) = C_1^{1/2} \left(C_1^{-1/2} C_2 C_1^{-1/2} \right)^s C_1^{1/2}. \tag{7}$$

The corresponding length of this path yields the following affine-invariant distance metric:

$$d_{\mathrm{AIRM}}(C_1, C_2) = \| \log(C_1^{-1/2} C_2 C_1^{-1/2}) \|_{\mathrm{F}} = \left[\sum_{i=1}^{d} \ln^2 \lambda_i (C_1^{-1} C_2) \right]^{1/2}. \tag{8}$$

where $\|\cdot\|_{\mathrm{F}}$ denotes the matrix Frobenius norm, and $\lambda_i(C_1^{-1} C_2)$ represents the generalized eigenvalues of the matrix pair (C_2, C_1).

2.3.2. Log-Euclidean geodesic and distance

Under the log-Euclidean metric (LEM), because the space of matrices is globally mapped to a vector space through the matrix logarithm, the geodesic curve corresponds to a simple linear interpolation within the transformed logarithmic domain as follows:

$$\eta_{\mathrm{LEM}}(t)=\exp\big((1-s)\log(C_1)+s\log(C_2)\big),\ s\in[0,1]. \tag{9}$$

The shortest distance separating C_1 and C_2 along this flat logarithmic trajectory is given explicitly by the Frobenius norm of their log-transformed difference

$$d_{\mathrm{LEM}}(C_1,C_2)=\|\log(C_1)-\log(C_2)\|_{\mathrm{F}}=\left\{\mathrm{tr}\left[\big(\log(C_1)-\log(C_2)\big)^2\right]\right\}^{1/2}. \tag{10}$$

2.4. Parameterized manifold curves and elastic actions

To extend analytical frameworks from isolated point evaluations to continuous shape analysis, parameter-dependent continuous curves mapping a one-dimensional scalar interval into the SPD manifold are considered. Such a curve is defined as $c(\xi):[\xi_{\min},\xi_{\max}]\to\mathcal{M}$, where ξ represents an arbitrary continuous parameter. Riemannian elastic shape analysis has been widely used to compute geodesics and distances between parameterized shapes while accounting for nonlinear reparameterization effects [34].

The velocity field, or the infinitesimal shape change of the curve at any parameter coordinate ξ, is given by its derivative $\dot{c}(\xi)$. This derivative is fundamentally constituted as a tangent vector lying in the localized tangent space

$$\dot{c}(\xi)=\frac{d}{d\xi}c(\xi)\in\mathcal{T}_{c(\xi)}\mathcal{M}. \tag{11}$$

Under the log-Euclidean flattening framework, this continuous curve is mapped to a trajectory of symmetric matrices, denoted as $\Psi(\xi)=\log(c(\xi))$. The derivative of this flattened continuous curve is given by

$$\dot{\Psi}(\xi)=\frac{d}{d\xi}\big(\log(c(\xi))\big)\in\mathcal{S}ym(d). \tag{12}$$

The magnitude of the local geometric variation along the parameterized domain is quantified via the metric tensor norm $\|\dot{\Psi}(\xi)\|_{\mathrm{F}}$. By defining a velocity vector field across the parameter axis, the global shape of the continuous curve can be scaled, stretched, and realigned via nonlinear reparameterization functions, while its intrinsic geometric properties on the manifold $\mathcal{M}$ are strictly preserved.

3. Proposed Riemannian manifold-valued trajectory modeling and elastic alignment framework

3.1. Localized sliding-window SPD trajectory generation

To preserve the continuous topological evolution of the full BIS and mitigate the limitations of conventional empirical frequency sub-band selection, a localized sliding-window framework is formulated.

Let the raw BIS captured on a specific inspection day, Day t ($t \in \{1,2,\ldots,T_{\max}\}$) consist of $K = 1000$ logarithmically spaced discrete frequency points. The measured parameters at each frequency point are the magnitude of impedance $Z_t(f)$ and the phase angle $\theta_t(f)$. A local temporal-frequency window of fixed length L slides across the entire spectrum with a unit step size. The resulting number of localized windows is $W = K - L + 1$.

For the w-th localized window, where the window index ranges across $w \in \{1,2,\ldots,W\}$, and the discrete frequency interval is bounded by $[w, w+L-1]$. To account for the variations in the orders of magnitude across the frequency spectrum, logarithmic and scale normalization operators are applied to construct the multivariate local feature matrix $X_w^t \in \mathbb{R}^{2\times L}$ as follows:

$$X_w^t = \begin{bmatrix} \log_{10}(Z_t(w)) & \log_{10}(Z_t(w+1)) & \ldots & \log_{10}(Z_t(w+L-1)) \\ \theta_t(w)/90^\circ & \theta_t(w+1)/90^\circ & \ldots & \theta_t(w+L-1)/90^\circ \end{bmatrix}. \tag{13}$$

To extract the underlying statistical correlations and joint variations between the normalized magnitude of impedance and phase within each localized frequency block, the sample covariance matrix is evaluated. To guarantee that the resulting matrix strictly satisfies the positive-definiteness boundary conditions on the Riemannian manifold, a Tikhonov regularization term εI is added, where $\varepsilon > 0$ is the covariance regularization coefficient. The localized status matrix $C_t(w) \in \mathcal{S}_{++}^2$ is formulated as

$$C_t(w) = \frac{1}{L-1}\sum_{i=1}^{L}\left(X_{w,i}^t - \bar{X}_w^t\right)\left(X_{w,i}^t - \bar{X}_w^t\right)^{\mathrm{T}} + \varepsilon I, \tag{14}$$

where $X_{w,i}^t \in \mathbb{R}^{2\times 1}$ denotes the i-th column vector of the feature matrix X_w^t, and $\bar{X}_w^t \in \mathbb{R}^{2\times 1}$ represents the local sample mean vector calculated as

$$\bar{X}_w^t = \frac{1}{L}\sum_{i=1}^{L} X_{w,i}^t. \tag{15}$$

Through this localized sliding mapping, the discrete one-dimensional BIS profile captured on Day t is successfully transformed into a continuous, multidimensional parameterized curve traversing the smooth nonlinear SPD manifold space $\mathcal{S}_{++}^2$, denoted as the Riemannian trajectory [35]:

$$c_t : \{1,2,\ldots,W\} \to \mathcal{S}_{++}^2. \tag{16}$$

Figure 1 illustrates the conversion from raw BIS local windows to SPD manifold points. By sliding the local window along the frequency axis, the full BIS profile is represented as a continuous Riemannian trajectory for subsequent alignment and degradation analysis.

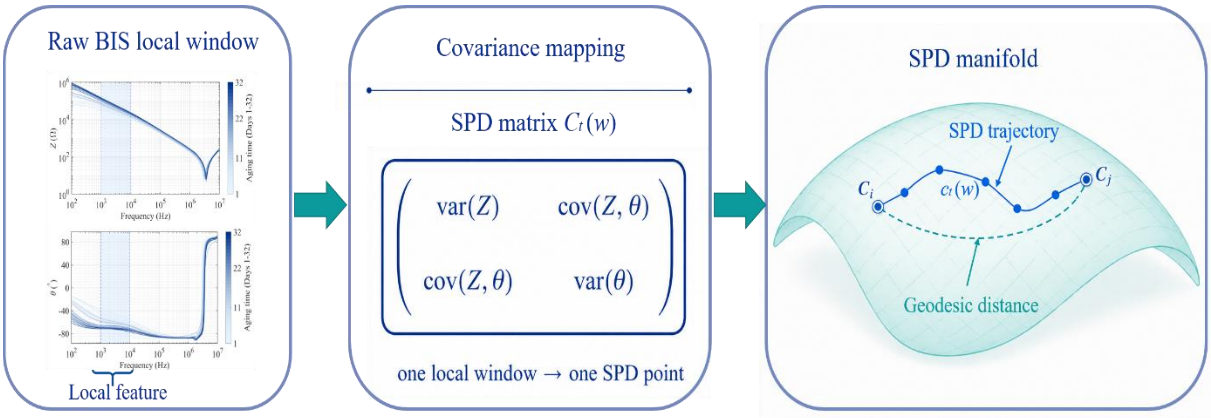

Figure 1. Localized SPD trajectory generation from raw BIS windows.

3.2. Log-domain velocity and SRVF coordinates

To achieve an elastic registration and comparison of the generated manifold curves, the parameterized trajectory $c_t(w)$ must be aligned to eliminate nonlinear frequency axis distortions. The continuous trajectory on the curved manifold is first globally projected into the flat vector space of real symmetric matrices $\mathcal{S}ym(2)$ via the matrix logarithmic map at the identity origin

$$\Psi_t(w) = \log(c_t(w)) \in \mathcal{S}ym(2), \quad w \in \{1,2,\ldots,W\}. \tag{17}$$

The velocity field representing the localized geometric modification rate of the trajectory with respect to the frequency window index axis is evaluated using a forward finite-difference numerical approximation as follows:

$$\dot{\Psi}_t(w) = \Psi_t(w+1) - \Psi_t(w), \quad w \in \{1,2,\ldots,N\}, \tag{18}$$

where $N = K - L = W - 1$ denotes the number of finite difference segments, or equivalently, the length of the resulting SRVF sequence.

To distinguish the standard analytical SRVF from its thresholded numerical representation, let $s \in [0,1]$ denote the continuous normalized trajectory parameter, and let $\Psi_t(s) = \log(c_t(s))$. The analytical SRVF is defined in the standard form as [36]

$$q_t(s) = \begin{cases} \dfrac{\dot{\Psi}_t(s)}{\sqrt{\|\dot{\Psi}_t(s)\|_{\mathrm{F}}}}, & \dot{\Psi}_t(s) \neq 0 \\ 0_{2\times 2}, & \dot{\Psi}_t(s) = 0 \end{cases}. \tag{19}$$

For any $q \in L^2([0,1], \mathrm{Sym}(2))$ and any admissible monotone reparameterization γ, the re-parameterization action is defined as

$$(\bar{q}_t^{\delta} \star \gamma)(s) = (q \circ \gamma)(s)\sqrt{\gamma'(s)} = q(\gamma(s))\sqrt{\gamma'(s)}. \tag{20}$$

For the standard analytical SRVF q_t, this action coincides with the SRVF representation of the re-parameterized trajectory $\Psi_t \circ \gamma$.

For the discrete numerical implementation, the finite-difference velocity in Eq (18) is normalized using a zero-velocity threshold. The thresholded discrete SRVF $q_t^{\delta}(w) \in \mathrm{Sym}(2)$ is defined as

$$q_t^{\delta}(w) = \begin{cases} \dfrac{\dot{\Psi}_t(w)}{\sqrt{\| \dot{\Psi}_t(w) \|_{\mathrm{F}}}}, & \| \dot{\Psi}_t(w) \|_{\mathrm{F}} > \delta \\ 0_{2\times 2}, & \text{otherwise} \end{cases}, \tag{21}$$

where δ is the SRVF zero-velocity threshold used to prevent numerical singularity.

To establish the continuous interpretation of the discrete representation, define the normalized grid $s_w = \dfrac{w-1}{N-1}, w = 1, 2, \ldots, N$ and let $\bar{q}_t^{\delta}(s)$ denote the piecewise-constant interpolation of $q_t^{\delta}(w)$

$$\bar{q}_t^{\delta}(s) = q_t^{\delta}(w), \qquad s \in [s_w, s_{w+1}], \quad w = 1, \ldots, N-1, \tag{22}$$

with $\bar{q}_t^{\delta}(1) = q_t^{\delta}(N)$. Thus $\bar{q}_t^{\delta} \in L^2([0,1], \mathrm{Sym}(2))$. Once the thresholded representation has been constructed, the subsequent elastic alignment acts directly on $\bar{q}_t^{\delta}$ through the right action defined in Eq (20). Proposition 1 in Section 3.6 shows that this action exactly preserves the L^2 norm for any fixed value of δ, even when the threshold suppresses some finite-difference velocity samples.

3.3. Log-Euclidean elastic alignment of manifold-valued trajectories

To separate the structural variations induced by heterogeneous cable geometry configurations, temperature fluctuations, different insulation materials, and spatial aging locations from the intrinsic material degradation of the polymer insulation, the SRVF trajectories are then aligned using an LE-DTW framework [37]. By executing elastic alignments on the manifold, this framework ensures a highly robust condition assessment that is universally applicable across varying physical operating environments.

Let $q_1^{\delta}(w)$ denote the baseline SRVF trajectory extracted from the absolute healthy condition of the cable (Day 1), and let $q_t^{\delta}(w)$ represent the test SRVF trajectory extracted from an unknown degradation state on Day *t*. A local distortion cost matrix $M_{\mathrm{cost}} \in \mathbb{R}^{N\times N}$ is formulated, where the geometric discrepancy at any arbitrary coordinate grid (i, j) is measured by the squared Frobenius norm of their log-flattened SRVF tensors as follows:

$$M_{\mathrm{cost}}(i, j) = \| q_1^{\delta}(i) - q_t^{\delta}(j) \|_{\mathrm{F}}^2, \quad i, j \in \{1, 2, \ldots, N\}. \tag{23}$$

To identify the optimal, nonlinear matching pathway that minimizes the cumulative structural mismatch energy, a cumulative distance matrix $D_{\mathrm{acc}} \in \mathbb{R}^{N\times N}$ is recursively evaluated via dynamic programming subject to monotonicity, continuity, and boundary conditions

$$D_{\mathrm{acc}}(i,j)=M_{\mathrm{cost}}(i,j)+\min\begin{cases}D_{\mathrm{acc}}(i-1,j)\\ D_{\mathrm{acc}}(i,j-1)\\ D_{\mathrm{acc}}(i-1,j-1)\end{cases}. \tag{24}$$

This computation is anchored by the initialization state $D_{\mathrm{acc}}(1,1)=M_{\mathrm{cost}}(1,1)$. The optimal time-warping function $\phi^*(w)$, which represents the reparameterization path mapping the frequency grid of the test curve back onto the reference coordinate system, is extracted through a global backtracking operation initializing from the terminal grid (N,N).

Following the optimization of $\phi^*(w)$, the highly coupled physical transformations within the raw BIS profile are orthogonally decoupled into the following two independent geometric metrics:

(1) Residual shape distance (D_{shape}): This metric measures the intrinsic, vertical geometric distortion remaining between the two manifold curves after all horizontal frequency axis shifts are entirely compensated. It serves as an uncompromised, location-, structure-, and material-invariant gauge of material dielectric degradation, providing extreme sensitivity to incipient microlevel insulation deterioration

$$D_{\mathrm{shape}}(t)=\sqrt{\frac{D_{\mathrm{acc}}(N,N)}{N}}. \tag{25}$$

(2) Alignment warping energy (E_{warp}): This metric calculates the integral area bounded between the nonlinear optimal warping pathway $\phi^*(w)$ and the ideal linear diagonal line representing zero frequency shift ($\phi(w)=w$). It captures the total horizontal resonance frequency drift caused by spatial parameter modifications, temperature variations, and structural heterogeneity

$$E_{\mathrm{warp}}(t)=\frac{1}{N}\sum_{w=1}^{N}|\ \phi^*(w)-w\,|. \tag{26}$$

3.4. CRSE and monotone state functional

Owing to the microchemical competing mechanisms between macromolecular chain scission and localized cross-linking reactions during thermal aging, the instantaneous trajectory distance $D_{\mathrm{shape}}(t)$ exhibits nonmonotonic fluctuations and local plateaus during the acceleration phase. To bridge the gap between geometric state distances and industrial prognostic requirements, an irreversible damage index is derived via the formulation of CRSE [38].

The discrete time-history integration of the squared shape distance is evaluated to construct the monotonically increasing damage function $\mathrm{CRSE}(t)$

$$\mathrm{CRSE}(t)=\sum_{\tau=1}^{t}\left(D_{\mathrm{shape}}(\tau)\right)^2. \tag{27}$$

By anchoring the terminal boundary conditions of the cable's lifecycle (where $T_{\max}$ represents complete dielectric breakdown and insulation failure), a normalized health index (HI) constrained strictly within a range of 0% to 100% is mapped as follows:

$$HI(t) = \left(1 - \frac{\mathrm{CRSE}(t) - \mathrm{CRSE}(1)}{\mathrm{CRSE}(T_{\max}) - \mathrm{CRSE}(1)}\right) \times 100\%. \tag{28}$$

3.5. RUL estimation via Riemannian feature-driven GPR

The normalized health index defined in Eq (28) provides an intuitive description of the complete degradation trajectory. However, its normalization requires the terminal value $\mathrm{CRSE}(T_{\max})$, which is available only after the cable has reached the experimentally defined end-of-life condition. Therefore, two distinct GPR-based evaluation protocols are considered in this study: A retrospective within-trajectory feature-mapping analysis and an independent cross-temperature RUL prediction experiment.

3.5.1. Retrospective within-trajectory feature mapping

For the retrospective analysis, the degradation feature vector is defined as follows:

$$F_{\mathrm{ret}}(t) = \begin{bmatrix} HI(t) & E_{\mathrm{warp}}(t) \end{bmatrix}^{\mathrm{T}}. \tag{29}$$

For a complete run-to-failure trajectory, the RUL percentage is

$$y(t) = \frac{T_{\max} - t}{T_{\max} - 1} \times 100\%. \tag{30}$$

Day-wise leave-one-out cross-validation (LOOCV) is used to compare different feature representations under identical GPR settings. Because both the normalized HI and the RUL labels are obtained from the completed trajectory of the same cable, this experiment is regarded only as a retrospective feature mapping analysis. Its results may be optimistic and thus are not used to demonstrate prognostic generalization to an unseen cable.

The retrospective evaluation also includes a chronologically constrained tail-holdout analysis, where the GPR model is trained on the earlier trajectory and tested on the final monitoring points. A training-referenced HI ensures that no normalization information is leaked from the held-out tail. Because all samples belong to the same completed cable, this analysis remains a retrospective within-trajectory evaluation rather than an independent cable-level validation.

3.5.2. Causal feature construction and cross-temperature prediction

To avoid introducing terminal failure information into the independent prognostic experiment, the normalized *HI* is retained only for retrospective degradation analysis and is not supplied to the GPR model in the cross-temperature prediction protocol. Instead, a causal cumulative degradation feature is defined as

$$G(t) = \log\left[1 + \mathrm{CRSE}(t) - \mathrm{CRSE}(1)\right]. \tag{31}$$

The feature $G(t)$ can be calculated using only the residual shape distances observed up to the current inspection time t. It does not require $T_{\max}$ and $\mathrm{CRSE}(T_{\max})$, future BIS measurements, or any RUL value of the cable being evaluated. The logarithmic transformation preserves the monotonic degradation ordering of CRSE while reducing its numerical dynamic range.

The alignment warping energy $E_{\mathrm{warp}}(t)$ is retained as a complementary descriptor of frequency axis distortion. Accordingly, the prognostic input vector is defined as

$$F_{\mathrm{casual}}(t) = [G(t) \quad E_{\mathrm{warp}}(t)] \in \mathbb{R}^{1\times 2}. \tag{32}$$

The complete run-to-failure trajectory obtained at 160 °C is used exclusively for training, whereas the independently aged cable at 140 °C is used exclusively for testing.

Let T_{160} denote the failure time of the training cable. Its RUL label is

$$y_{160}(t) = \frac{T_{160} - t}{T_{160} - 1} \times 100\%, \qquad t = 1, \ldots, T_{160}, \tag{33}$$

where $y_{160}(t)$ is the RUL percentage of the training cable on Day t.

The training dataset $\mathcal{D}_{\mathrm{tr}}$ is

$$\mathcal{D}_{\mathrm{tr}} = \left\{ \left(F_{160,\mathrm{causal}}(t), y_{160}(t) \right) \right\}_{t=1}^{T_{160}}, \tag{34}$$

where $F_{160,\mathrm{causal}}(t) = \left[G_{160,t} \quad E_{\mathrm{warp},160}(t) \right]^{\mathrm{T}}$. For the unseen 140 °C cable, the test feature at time t is

$$F_{140,\mathrm{causal}}(t) = \left[G_{140,t} \quad E_{\mathrm{warp},140}(t) \right]^{\mathrm{T}}. \tag{35}$$

All feature-standardization parameters and GPR hyperparameters are determined exclusively from the 160 °C training data. No RUL label, failure time, terminal CRSE value, future BIS measurement, or previous RUL value from the 140 °C cable is used during training or prediction. Its failure time is used only after prediction to construct the ground truth RUL for evaluation.

3.5.3. Gaussian process regression

For either evaluation protocol, let the corresponding GPR training dataset be denoted as $\mathcal{D}_{\mathrm{tr}} = \left\{ \left(F_i, y_i \right) \right\}_{i=1}^{N_{\mathrm{tr}}}$, where N_{tr} is the number of training samples. For the retrospective analysis, $\mathcal{D}_{\mathrm{tr}}$ contains the remaining samples in the current leave-one-out fold, and the held-out feature is used for testing. For the cross-temperature experiment, $\mathcal{D}_{\mathrm{tr}} = \mathcal{D}_{\mathrm{tr}}^{\mathrm{cross}}$ in Eq (34), and the test features are given by Eq (35).

A Gaussian process regression model is established to achieve nonparametric Bayesian regression over the Riemannian feature domain [39]. The latent mapping function $f(F)$ is assigned a zero-mean Gaussian process $\mathcal{G}$ prior governed by a spatial covariance kernel function $k(F, F')$

$$f(F) \sim \mathcal{G}\left(0, k(F, F')\right). \tag{36}$$

To accurately capture the nonlinear correlation between distinct Riemannian feature states, a squared exponential kernel equipped with automatic relevance determination (ARD) is used

$$k(F,F') = \sigma_f^2 \exp\left(-\frac{1}{2}(F-F')\Lambda^{-2}(F-F')^{\mathrm{T}} \right). \tag{37}$$

where σ_f^2 denotes the signal variance parameter controlling the overall vertical amplitude. The diagonal matrix $\Lambda = \mathrm{diag}(l_G, l_{\mathrm{warp}})$ contains the independent length scales corresponding to the $G(t)$ and E_{warp} dimensions. Within the ARD mechanism, the precision weight matrix Λ^{-2} autonomously optimizes the relevance of each decoupled feature during the regression process.

Let K_{tr} denote the covariance matrix of the training features and let k_* denote the covariance vector between a test feature F_* and the training features. The predictive mean μ_* and the epistemic predictive variance σ_*^2 are inferred as follows:

$$\mu_* = k_*^{\mathrm{T}} \left(K_{\mathrm{tr}} + \sigma_n^2 \mathrm{I} \right)^{-1} y_{\mathrm{tr}}, \tag{38}$$

$$\sigma_*^2 = k(F_*, F_*) - k_*^{\mathrm{T}} \left(K_{\mathrm{tr}} + \sigma_n^2 \mathrm{I} \right)^{-1} k_* . \tag{39}$$

where $y_{\mathrm{tr}} = \left[y_1, y_2, \ldots, y_{N_{\mathrm{tr}}} \right]^{\mathrm{T}}$ denotes the aggregated column vector of historical training labels, $k(F_*, F_*)$ is the prior variance at the test feature, and σ_{n}^2 signifies the estimated measurement noise variance.

Within this probabilistic framework, the predictive mean μ_* represents the expected remaining lifespan, while the predictive variance σ_*^2 quantifies the associated epistemic uncertainty, naturally forming the 99% predictive interval to evaluate the estimation reliability.

The corresponding 99% predictive interval is

$$\left[\mu_* - 2.576\sigma_{y,*}, \mu_* + 2.576\sigma_{y,*} \right], \tag{40}$$

$$\sigma_{y,*}^2 = \sigma_*^2 + \sigma_n^2 . \tag{41}$$

Finally, to strictly adhere to real-world degradation boundaries, the mathematical expectation μ_* is constrained to the valid physical domain of $[0\%, 100\%]$ using an industrial bounding operator, yielding the following definitive prognostic output $\hat{y}_*$:

$$\hat{y}_* = \max\left(0, \min\left(100, \mu_* \right) \right). \tag{42}$$

3.6. Mathematical properties and computational complexity

To further clarify the mathematical structure of the proposed Riemannian elastic alignment framework, the admissible reparameterization space, continuous alignment objective, invariance property, monotonicity of CRSE, and computational complexity are analyzed in this subsection.

The admissible reparameterization functions are defined on the normalized window index domain, where $s \in [0,1]$ denotes the continuous normalized trajectory parameter. Let Γ denote the following set of strictly increasing and boundary-preserving mappings:

$$\Gamma = \{\gamma : [0,1] \to [0,1] \mid \gamma(0) = 0, \gamma(1) = 1, \gamma'(s) > 0\}. \tag{43}$$

The endpoint constraints ensure that the initial and terminal window positions are consistently aligned, while the positivity condition preserves the ordering of the frequency axis and prevents folding of the trajectory.

Based on the interpolated thresholded SRVF representation introduced in Section 3.2, a continuous elastic interpretation of the proposed alignment is formulated as follows:

$$\gamma^* = \arg\min_{\gamma\in\Gamma} \left[\int_0^1 \left\| \bar{q}_1^{\delta}(s) - (\bar{q}_t^{\delta} \star \gamma)(s) \right\|_{\mathrm{F}}^2 ds + \lambda \int_0^1 (\sqrt{\gamma'(s)} - 1)^2 ds \right]. \tag{44}$$

where $\bar{q}_1^{\delta}$ denotes the piecewise-constant interpolation of the thresholded discrete SRVF of the baseline trajectory, and $\bar{q}_t^{\delta}$ denotes that of the trajectory at aging state t. The first term measures the elastic mismatch between the two thresholded SRVF representations under the right reparameterization action defined in Eq (20). The parameter $\lambda \geq 0$ is included in the general formulation to penalize excessive local stretching or compression.

By minimizing over all admissible mappings in Γ, the elastic distance between two SPD-valued trajectories can be defined as

$$d_{\mathrm{el}}(c_1, c_t) = \inf_{\gamma\in\Gamma} \left\| \bar{q}_1^{\delta} - \bar{q}_t^{\delta} \star \gamma \right\|_{L^2}. \tag{45}$$

This distance defines the continuous elastic comparison directly on the interpolated thresholded SRVF representations corresponding to the discrete sequences used in the proposed LE-DTW procedure.

Equations (38) and (39) provide a continuous elastic interpretation of the thresholded SRVF representation used in the proposed method. Thresholding is first applied during the construction of q_t^{δ}, and the subsequent alignment then acts on the resulting fixed representation $\bar{q}_t^{\delta}$. As established in Proposition 1, the right-hand reparameterization action defined in Eq (20) exactly preserves the L^2 norm of $\bar{q}_t^{\delta}$ for any fixed threshold δ.

Proposition 1. L^2 norm invariance of the reparameterization action on the thresholded SRVF representation.

Let $\bar{q}^{\delta} \in L^2([0,1], \mathrm{Sym}(d))$ be an interpolated thresholded SRVF representation constructed using an arbitrary fixed threshold $\delta \geq 0$, and let $\gamma \in \Gamma$. Under the right-hand re-parameterization action, the L^2 norm is preserved

$$\left\| \bar{q}^{\delta} \star \gamma \right\|_{L^2} = \left\| \bar{q}^{\delta} \right\|_{L^2}. \tag{46}$$

Indeed, we have

$$\begin{aligned} \left\| \bar{q}^{\delta} \star \gamma \right\|_{L^2}^2 &= \int_0^1 \left\| \bar{q}^{\delta}(\gamma(s)) \right\|_{\mathrm{F}}^2 \gamma'(s) ds \\ &= \int_0^1 \left\| \bar{q}^{\delta}(u) \right\|_{\mathrm{F}}^2 du = \left\| \bar{q}^{\delta} \right\|_{L^2}^2 \end{aligned}, \tag{47}$$

where $u=\gamma(s)$. Therefore, the norm-preserving property holds for any fixed threshold δ, including the case in which the threshold suppresses some nonzero finite-difference velocity samples. The proof only requires $\bar{q}^{\delta}\in L^2$ and does not require $\bar{q}^{\delta}$ to coincide with the unthresholded analytical SRVF.

Proposition 2. Perturbation stability.

For two trajectory pairs (c_1,c_t) and $(\tilde{c}_1,\tilde{c}_t)$, the change in the elastic distance is bounded by the perturbations of the two inputs as follows:

$$\left|d_{\mathrm{el}}(c_1,c_t)-d_{\mathrm{el}}(\tilde{c}_1,\tilde{c}_t)\right|\le d_{\mathrm{el}}(c_1,\tilde{c}_1)+d_{\mathrm{el}}(c_t,\tilde{c}_t)\,. \tag{48}$$

This inequality is obtained from the reverse triangle inequality. It indicates that small perturbations in the SPD trajectories lead to bounded changes in the proposed elastic distance.

The CRSE constructed in Section 3.4 is monotonic because each increment is defined by a non-negative squared residual shape distance. Specifically, we have

$$\mathrm{CRSE}(t)=\sum_{\tau=1}^{t}D_{\mathrm{shape}}^{2}(\tau)\,, \tag{49}$$

$$\mathrm{CRSE}(t)-\mathrm{CRSE}(t-1)=D_{\mathrm{shape}}^{2}(t)\ge 0\,. \tag{50}$$

Therefore, although the instantaneous residual shape distance $D_{\mathrm{shape}}(t)$ may fluctuate due to local dielectric changes and measurement variations, the accumulated CRSE provides a monotonic state functional for the evolution of degradation.

Finally, the computational complexity is analyzed. For W localized SPD matrices and $N=W-1$ SRVF samples, the matrix logarithm operations require $O(Wd^3)$ time. The pairwise SRVF cost calculation and dynamic programming alignment require $O(N^2d^2)$ time, while the accumulated cost matrix requires $O(N^2)$ memory. Therefore, the overall time and memory complexities are

$$\mathcal{T}(W,N,d)=O\left(Wd^3+N^2d^2\right), \tag{51}$$

$$\mathcal{M}(W,N,d)=O\left(Wd^2+N^2\right). \tag{52}$$

Since the present application uses low-dimensional covariance matrices, the main computational burden comes from the dynamic programming stage. In practical applications, a band-constrained search can be further adopted when the maximum admissible frequency axis distortion is known.

3.7. Algorithmic implementation

Algorithm 1 summarizes the complete computational procedure of the proposed Riemannian manifold-valued trajectory modeling and elastic alignment framework. The algorithm includes localized SPD covariance construction, log-Euclidean mapping, SRVF representation, LE-DTW-based trajectory alignment, CRSE accumulation, HI construction, and optional GPR-based RUL prediction.

The numerical implementation settings of the proposed framework are provided in the Appendix.

Algorithm 1. Riemannian manifold-valued trajectory modeling and elastic alignment framework	
Input	Measured cable responses $\{Y_t\}_{t=1}^{T_{\max}}$, $Y_t = \left\{\left(f_i, Z_{t,i}, \theta_{t,i}\right)\right\}_{i=1}^{K}$; baseline Y_1; L, ε, δ.
Output	$\phi^*(w)$, $D_{\text{shape}}(t)$, $E_{\text{warp}}(t)$, $\text{CRSE}(t)$, $HI(t)$, $G(t)$, optional $\hat{y}_t$.
1	Set $W = K - L + 1$, $N = W - 1 = K - L$.
2	Construct the regularized local covariance matrices $C_t(w)$ from overlapping windows of Y_t.
3	Assemble $C_t(w)$ into the SPD-valued trajectories $c_t = \{C_t(w)\}_{w=1}^{W}$.
4	Map c_t to the log-Euclidean domain and obtain the SRVF representations q_t^δ.
5	Align each q_t^δ with the healthy baseline q_1^δ using LE-DTW and obtain the optimal warping paths $\phi^*(w)$.
6	Compute $D_{\text{shape}}(t)$ and $E_{\text{warp}}(t)$ from the alignment results.
7	Construct $\text{CRSE}(t) = \sum_{\tau=1}^{t}\left(D_{\text{shape}}(\tau)\right)^2$, normalize it into $HI(t)$ for retrospective analysis, and calculate the causal cumulative feature $G(t)$.
8	Form $F_{\text{ret}}(t) = [HI(t), E_{\text{warp}}(t)]$ for retrospective mapping and $F_{\text{casual}}(t) = [G(t), E_{\text{warp}}(t)]$ for independent prediction.
9	If RUL prediction is required, train the GPR model using $F(t)$ and obtain the bounded prediction $\hat{y}_t \in [0,100]\%$
10	Return $\phi^*(w)$, $D_{\text{shape}}(t)$, $E_{\text{warp}}(t)$, $\text{CRSE}(t)$, $HI(t)$, $G(t)$, and optional $\hat{y}_t$.

4. Cable degradation as an application

4.1. Cable aging test

The tested specimen was a shielded single-core motor connection cable used in motor drive applications. Its detailed electrical and physical specifications, including the insulation material, rated voltage, conductor cross-section, cable length, outer diameter, shielding structure, and conductor material, are summarized in Table 1. The cable had a total length of 109.4 cm and an outer diameter of 17.1 mm, as shown in Figure 2. The cable consisted of a bare copper conductor with a cross-sectional area of 50 mm², an inner black PVC insulation layer, a tinned-copper shielding braid, and an orange PVC outer sheath. The electrical measurements were taken at the shielding braid location, allowing the degradation behavior of the insulation system to be evaluated during thermal aging.

Table 1. Detailed electrical and physical specifications of the cable and motor used for the test.

Motor		Cable	
Parameters	Values	Parameters	Values
Rated power	30 kW	Outer diameter	17.1 mm
		Conductor cross-section	50 mm^2
Rated speed	2800 rpm	Length	109.4 cm
		Rated voltage	600 V
Rated DC link voltage	270 V	Shielding mesh	Tinned copper
		Interior insulation material (black)	PVC
Rated AC voltage	190 V	External insulation material (orange)	PVC
		Conductor material	Bare copper

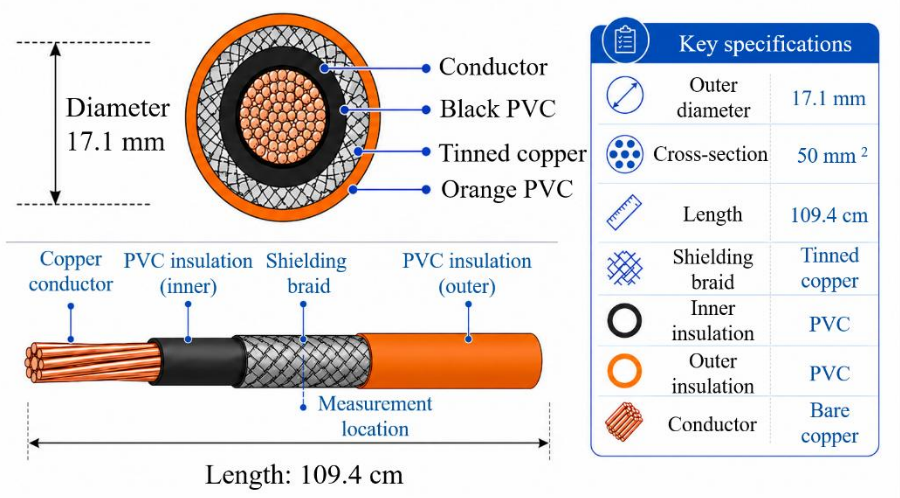

Figure 2. Structure and key specifications of the tested shielded PVC-insulated cable.

The cable sample was placed in a high-temperature chamber and continuously exposed to 120/140/160 °C to accelerate degradation of the insulation. The measuring instruments were installed outside the oven, and the in-oven cable specimen was connected to the impedance analyzer through heat-resistant leads suitable for temperatures above 300 °C. BIS was then carried out using a Keysight E4990A impedance analyzer over a frequency range from 100 Hz to 10 MHz, with 1000 logarithmically spaced frequency points. This configuration enabled the dielectric response of the cable insulation to be characterized over both the low-frequency polarization region and the high-frequency resonance-related region. Before each BIS measurement, open-short compensation was conducted, and the cable was firmly fixed to reduce measurement uncertainty and improve repeatability.

In addition to BIS, insulation resistance and partial discharge inception voltage (PDIV) measurements were included in the monitoring procedure. The insulation resistance was measured under a DC voltage of 1000 V using a Keysight U1461A insulation multimeter. The complete measurement workflow is illustrated in Figure 3. During the aging process, impedance spectra were acquired periodically, followed by an assessment of insulation failure. If the cable did not meet the failure criterion, the sample was returned to the aging loop for continued thermal exposure. The experiment lasted for 52/32/18 working days and was stopped when the insulation resistance decreased below 1 MΩ, which was defined as the end-of-life condition of the cable insulation.

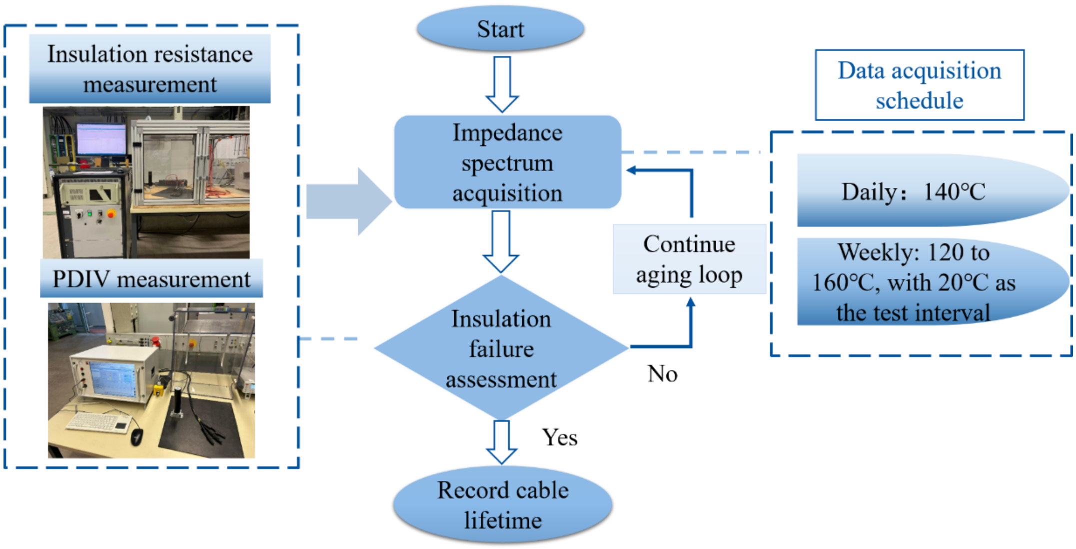

Figure 3. Experimental measurement workflow for thermal aging and assessment of insulation degradation.

4.2. Experimental setup

Two complementary types of validation are considered: Retrospective within-trajectory evaluation and independent cross-temperature prediction. The retrospective evaluation includes both day-wise LOOCV and chronologically constrained tail-holdout validation.

Day-wise LOOCV. Cable run-to-failure experiments are destructive, costly, and time-consuming, and a complete accelerated aging test generally requires approximately 3–6 months. Therefore, the number of available degradation trajectories is limited. Day-wise LOOCV is adopted as a data-efficient protocol that allows nearly all observations to be used for training while ensuring that each monitoring day is tested once.

For the t-th fold, the feature vector and RUL label of Day t are excluded, and the GPR model is trained using $\mathcal{D}_{-t} = \left\{\left(F(s), y(s)\right) : s \neq t\right\}$. The trained model then estimates $y(t)$ using only the held-out feature vector $F(t)$. Therefore, this protocol is used only to compare the relative within-trajectory mapping capability of different feature representations and is not interpreted as independent prognostic validation.

In this experiment, the RUL labels and the normalized HI are constructed from the complete run-to-failure trajectory. In particular, the original HI uses $\mathrm{CRSE}(T_{\max})$ as its terminal normalization value. Therefore, the LOOCV results represent a retrospective within-trajectory comparison rather than strictly causal online prediction. Nevertheless, all feature inputs, including raw BIS, D_{shape},

E_{warp}, $D_{\text{shape}}+E_{\text{warp}}$, HI, and the proposed $\text{HI}+E_{\text{warp}}$, are evaluated using identical folds, GPR settings, and evaluation metrics. Consequently, this protocol provides a fair comparison of the relative degradation information contained in the different feature representations. The original manuscript already described the use of one held-out day and the remaining days for training.

Chronologically constrained tail-holdout validation. To further evaluate the model under a temporally ordered prediction setting, an additional tail-holdout experiment is performed. Let t denote the final day of the training period. The training and testing sets are defined as follows:

$$\mathcal{D}_{\text{tr}}^{(t)}=\left\{\left(F(\tau),y(\tau)\right)\right\}_{\tau=1}^{t}\ \mathcal{D}_{\text{te}}^{(t)}=\left\{\left(F(\tau),y(\tau)\right)\right\}_{\tau=t+1}^{T_{\max}}. \tag{53}$$

The training cutoff is selected as $T_{\max}-t$, corresponding to prediction of the final t monitoring days, respectively. Unlike day-wise LOOCV, all test samples occur after the training period.

For each setting, the HI normalization scale, feature-standardization parameters, and GPR hyperparameters are determined exclusively from Days 1 to t. The feature vector is $F^{(t)}(\tau)=\left[\text{HI}^{(t)}(\tau),E_{\text{warp}}(\tau)\right]$, where $\text{HI}^{(t)}$ is calculated using a normalization scale obtained only from the training period, rather than the terminal value $\text{CRSE}(T_{\max})$. At a held-out day $\tau>t$, the available quantities include the current BIS measurement, the healthy baseline, the fixed training-derived normalization parameters, and the trained GPR model. The held-out RUL label, subsequent BIS measurements, and any normalization information derived from the held-out tail are not used during model fitting.

Because RUL labels from the earlier portion of the same completed cable trajectory are used for training, this protocol remains a retrospective within-trajectory extrapolation experiment, even though the held-out points are temporally later than all training samples.

For the degradation and RUL experiments, a healthy Day 1 SPD trajectory is used as the reference for LE-DTW alignment. It is selected before accelerated degradation and represents the initial healthy insulation state. Therefore, it provides a physically interpretable baseline from which subsequent frequency axis distortion and residual geometric degradation can be measured.

Independent cross-temperature validation. To evaluate RUL prediction without using any target information from the tested cable, the complete run-to-failure trajectories obtained at 160 °C are used exclusively for GPR training, whereas the independently aged cables at 140 °C are used exclusively for testing. Separate experiments are conducted for the 1-m, 2-m, and 3-m cables. For each cable length, the training and test features are defined as $F_{160,\text{causal}}(t)=\left[G_{160}(t),E_{\text{warp},160}(t)\right]^{\text{T}}$ and $F_{140,\text{causal}}(t)=\left[G_{140}(t),E_{\text{warp},140}(t)\right]^{\text{T}}$, respectively. Feature standardization parameters, kernel parameters, and GPR hyperparameters are determined exclusively from the 160 °C training data and are applied unchanged to the 140 °C test data.

No RUL label, failure time, terminal CRSE value, future BIS measurement, or previously observed RUL value from the 140 °C cables is used during model training or prediction. Their experimentally observed failure times are used only after prediction to construct the ground truth RUL values and calculate root mean square error (RMSE), mean absolute error (MAE), and R^2.

5. Numerical analysis of the cable application

5.1. Raw BIS evolution and Riemannian trajectory representation

Figure 4 shows the raw BIS evolution during thermal aging. Although the magnitude of impedance and phase angle vary with aging time, the degradation trend is not sufficiently clear in the original frequency domain. The responses exhibit strong frequency dependence, local curve overlap, and pronounced high-frequency resonance shifts. These effects make indicators based on fixed frequency points, selected sub-bands, or direct Euclidean comparisons vulnerable to peak misalignment and nonmonotonic fluctuations.

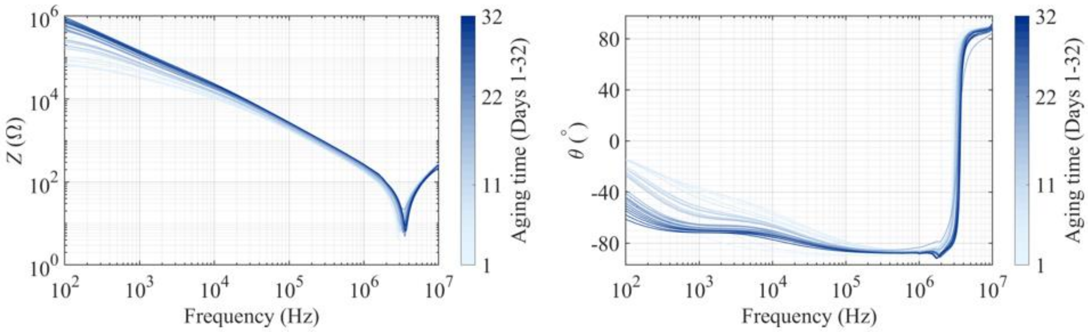

Figure 4. Evolution of raw BIS during thermal aging.

To obtain a more structured representation, the raw BIS curves are converted into SPD trajectories using the localized sliding-window strategy. As shown in Figure 5, each aging state is represented as a continuous trajectory in the Riemannian feature space, where local impedance variance, phase variance, and their covariance jointly characterize the broadband dielectric response. Compared with the raw BIS curves, the SPD trajectory representation better preserves the coupled evolution of magnitude and phase and reorganizes BIS into a compact geometric form.

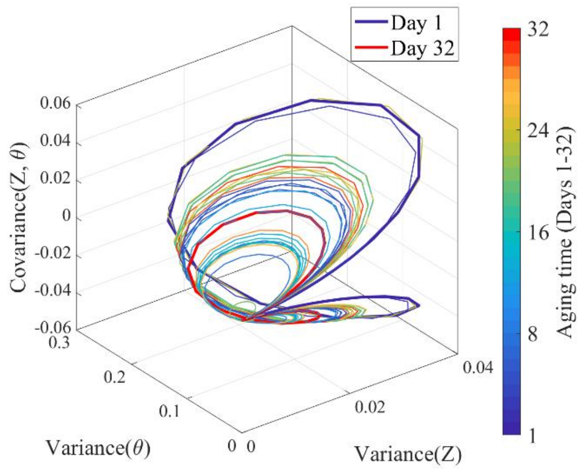

Figure 5. Riemannian SPD trajectory representation of BIS profiles during thermal aging.

However, the Riemannian trajectories are still not strictly monotonic during aging, since resonance drift and local dielectric fluctuations remain coupled with material degradation. Therefore, this representation does not directly provide a final health indicator, but it offers a suitable geometric basis for the subsequent Riemannian DTW-based elastic alignment and degradation feature extraction.

5.2. Response of the general method to controlled cable perturbations

5.2.1. Length-induced reparameterization

Cable length is first investigated because it directly changes the distributed electrical parameters of the cable, such as equivalent resistance, inductance, capacitance, and conductance. These changes can shift the frequency response of BIS and may cause geometry-induced variations to be incorrectly interpreted as insulation degradation.

As shown in Figure 6, the magnitude of impedance in the 1-m, 2-m, and 3-m cables exhibits a similar overall decreasing trend with increasing frequency. However, length-dependent differences are still observed, especially in the low-frequency magnitude of impedance and the phase response. In the phase spectra, the longer cables show noticeable deviations in the low-frequency region, while the high-frequency resonance transition remains strongly affected by the distributed cable parameters. These results indicate that cable length introduces additional spectral distortion in both Z and θ, making direct comparisons in the raw frequency domain unreliable.

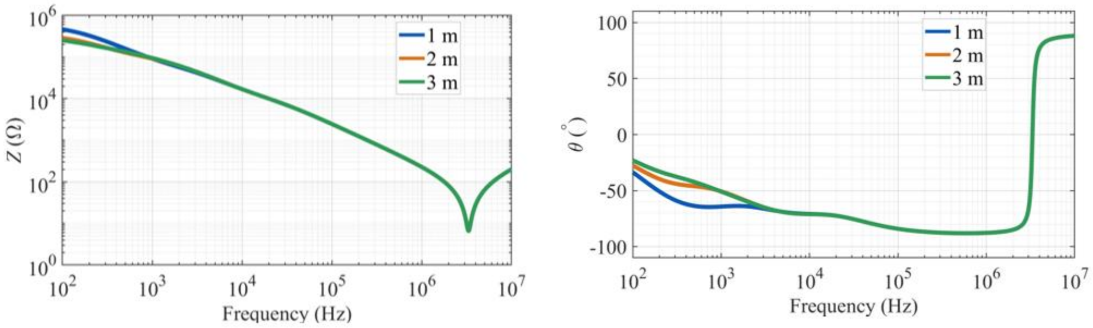

Figure 6. Raw BIS responses of cables with different lengths on Day 10.

Figure 7 presents the decoupling results obtained from the Riemannian DTW framework. In the right-hand panel, the diagonal dashed line represents the ideal case without frequency axis distortion. The optimal warping paths $\phi^*(w)$ of the 1-m, 2-m, and 3-m cables clearly deviate from this baseline, indicating that cable length introduces nonlinear horizontal misalignment in the BIS trajectories. The deviations are particularly evident in the low-to-middle window index range, approximately below w = 700, where the warping paths show strong nonlinear bending and local staircase-like behavior. In contrast, the paths gradually approach the diagonal baseline in the high-index region.

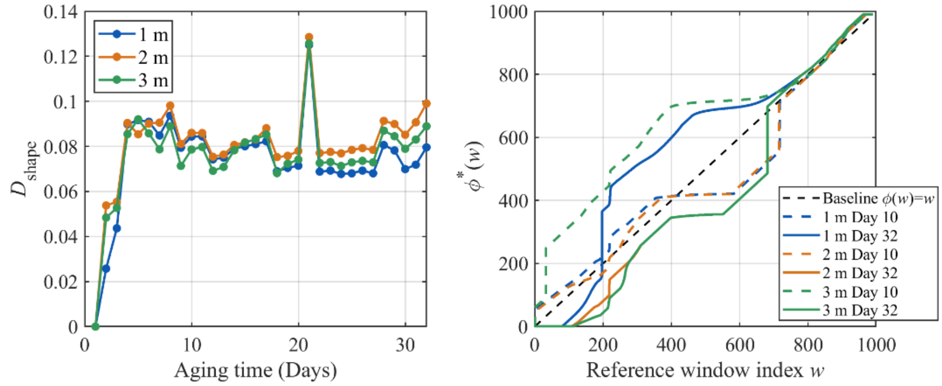

Figure 7. Riemannian decoupling results for cables with different lengths.

The left-hand panel shows D_{shape}, which quantifies the remaining aging-related geometric difference after frequency axis alignment. Although the 1-m, 2-m, and 3-m cables have different warping paths, their D_{shape} curves remain close and show a similar evolution trend, including the common peak around Day 21. This indicates that length-induced spectral shifts are mainly absorbed by $\phi^*(w)$, while D_{shape} still preserves the insulation aging information. Therefore, the proposed method provides a length-robust assessment of cable degradation.

5.2.2. Temperature-dependent domain shift

To evaluate the method's generalizability across diverse operational severities, thermal aging tests were conducted under three temperature conditions: 120 °C, 140 °C, and 160 °C. The 120 °C sample was monitored for 52 days without evident aging failure, the 140 °C sample was aged for 32 days, and the 160 °C sample showed accelerated degradation within 18 days. This comparison is used to verify whether the proposed method can distinguish true temperature-accelerated insulation degradation from temperature-induced spectral distortion.

Figure 8 shows that the raw BIS responses are strongly affected by aging temperature. In the spectra of the magnitude of impedance, the overall broadband decay is similar, but the curve's spread is temperature-dependent. The 120 °C curves exhibit a narrower distribution in both Z and θ, which is consistent with the fact that no evident aging is observed after 52 days during the measurement. In contrast, the 160 °C curves show a wider evolution range and a clear shift of the high-frequency resonance toward higher frequencies. This indicates that elevated temperature not only accelerates dielectric degradation but also modifies the resonance-related frequency response.

Figure 9 presents the Riemannian decoupling results under the three temperatures. The optimal warping paths $\phi^*(w)$ clearly deviate from the diagonal baseline, confirming that temperature variation causes nonlinear frequency axis misalignment. The 160 °C paths show stronger staircase-like deformation, indicating more severe spectral restructuring under high thermal stress. By contrast, the 120 °C paths are relatively smoother, corresponding to the absence of obvious aging-related failure during the test.

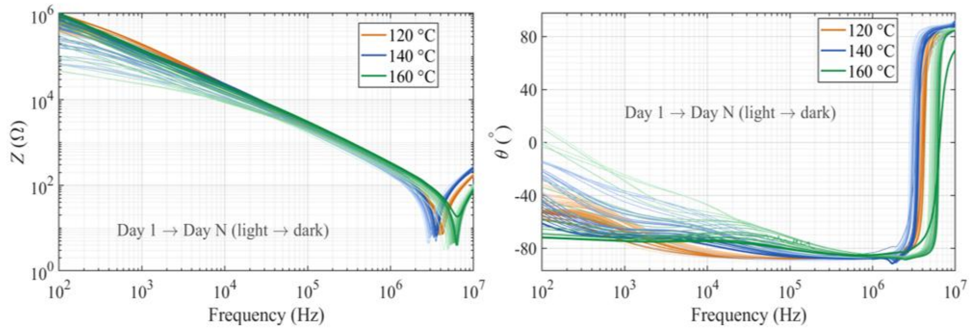

Figure 8. Raw BIS responses under different aging temperatures on Day 10.

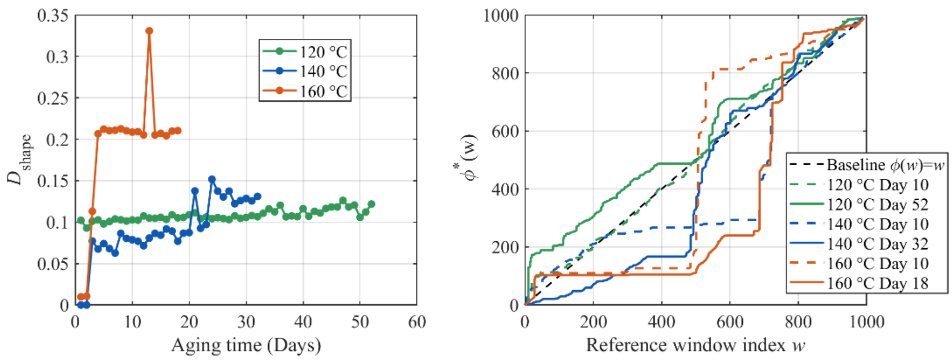

Figure 9. Riemannian decoupling results for cables with different aging temperatures.

The residual shape distance D_{shape} quantifies the remaining degradation-related geometric difference after temperature-induced frequency axis shifts are compensated. The 160 °C curve stays at a relatively high level during the 18-day test, indicating rapid deviation of the insulation state from the healthy reference under severe thermal aging. The 120 °C curve remains relatively stable over 52 days; its nonzero amplitude mainly reflects the temperature-dependent dielectric offset relative to the 140 °C healthy reference, while the slight temporal increase suggests that early-stage dielectric changes can still be monitored under mild thermal stress. The 140 °C result lies between these two cases, showing moderate progression of aging. These results also indicate that $\phi^*(w)$ mainly captures temperature-induced spectral shifts, while D_{shape} preserves the residual aging-related geometric changes.

5.2.3. Spatially localized perturbation

To evaluate the influence of spatially nonuniform degradation, three aging scenarios are considered: Uniform aging, middle-section accelerated aging, and dual-end accelerated aging. As shown in Figure 10, the aging location clearly affects the raw BIS evolution, especially in the low-frequency range (<10 kHz).

For the magnitude of impedance, all cases show a similar broadband decreasing trend with frequency, while local differences appear mainly in the low-frequency region and around the resonance valley. For the phase response, specifically, the dual-end concentrated aging scenario exhibits higher sensitivity in the phase shift compared with the case of uniform aging, as the degradation near the measurement terminals is more directly coupled to the input impedance. In contrast, the middle-section aging case shows a relatively moderate change in both magnitude and phase, since the healthier terminal sections reduce the direct influence of central degradation on the measured port response.

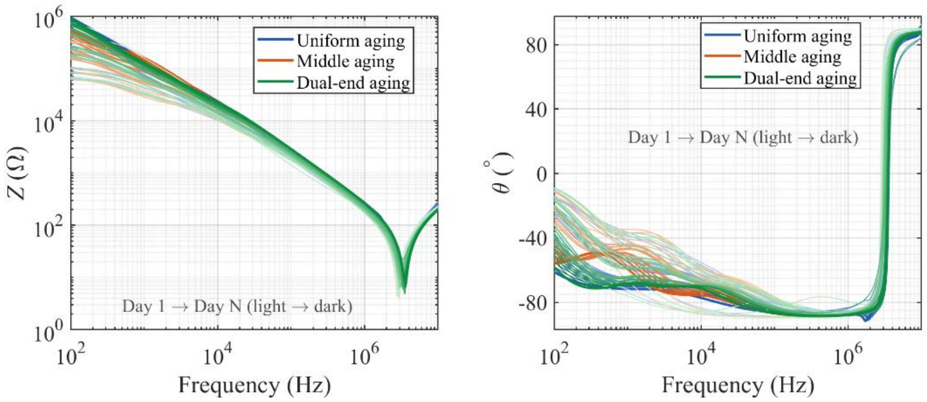

Figure 10. Raw BIS responses under different aging locations on Day 10.

Figure 11 shows the Riemannian decoupling results for different aging locations. The optimized warping path $\phi^*(w)$ in the right-hand panel describes the horizontal frequency window distortion caused by spatially nonuniform degradation. Compared with the case of uniform aging, the cases of middle-aging and dual-end aging exhibit different warping patterns, with more evident local staircase-like changes. This indicates that localized degradation changes the spectral alignment relationship through position-dependent impedance discontinuities and reflection effects.

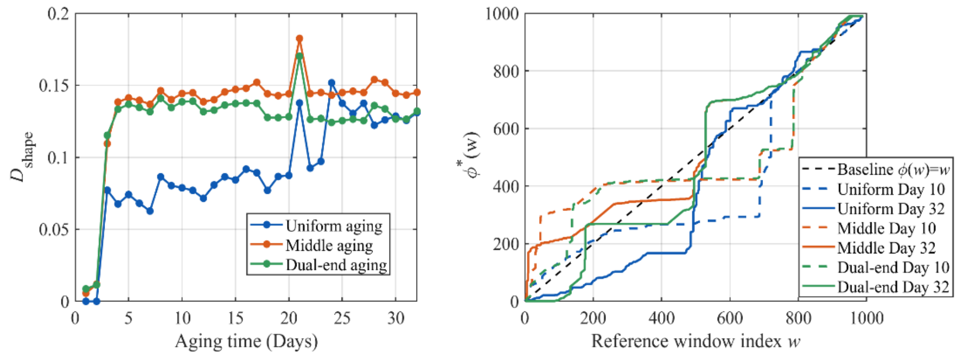

Figure 11. Riemannian decoupling results for cables with different aging locations.

The residual shape distance D_{shape} in the left-hand panel quantifies the remaining geometric difference after this elastic alignment. The cases of middle-aging and dual-end aging exhibit higher D_{shape} values than uniform aging over most aging days, showing that localized degradation produces stronger residual changes in the SPD trajectory. Meanwhile, all three cases exhibit clear evolution of D_{shape} with aging time, indicating that the proposed metric can still identify insulation aging under different degradation locations. Therefore, the proposed method separates location-induced spectral distortion from degradation-related geometric variation.

5.3. HI construction and retrospective within-trajectory mapping

The previous results show that D_{shape} can describe the residual degradation-related geometric difference after Riemannian alignment, while $\phi^{*}(w)$ captures frequency axis distortion. However, D_{shape} is an instantaneous metric and may still contain local fluctuations. Therefore, CRSE is introduced to convert the fluctuating residual distance into a monotonic damage descriptor.

As shown in Figure 12, CRSE increases monotonically with aging time by accumulating the squared D_{shape} values. This indicates that local geometric deviations are progressively integrated into irreversible degradation energy. Based on the CRSE, the normalized HI is further constructed, decreasing from 100% in the initial healthy state to 0% at the end-of-life condition. Compared with the instantaneous D_{shape}, the normalized HI provides a smooth retrospective representation of the completed degradation trajectory and is used as an input to the within-trajectory feature mapping analysis.

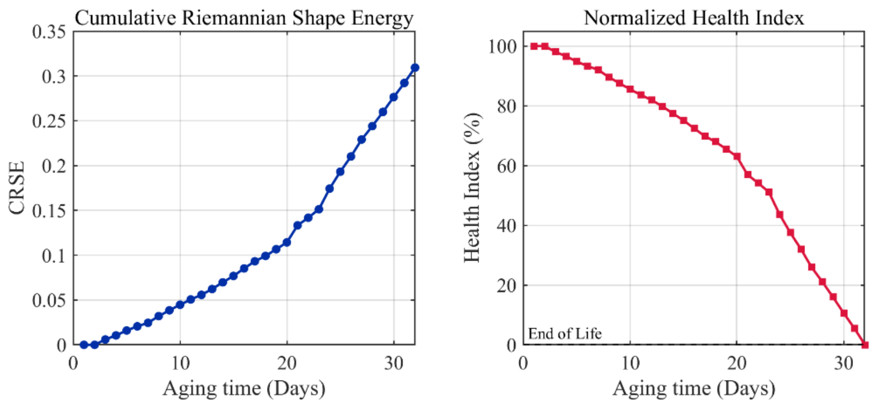

Figure 12. CRSE and normalized HI during thermal aging at 140 °C.

For retrospective RUL mapping, the normalized HI and the warping energy derived from $\phi^{*}(w)$ are used as two complementary Riemannian degradation features. The former reflects the accumulated insulation degradation state after CRSE mapping, while the latter quantifies the frequency axis distortion absorbed during elastic matching. As shown in Figure 13, the predicted RUL follows the decreasing trend of the target RUL, and the 99% predictive interval provides an uncertainty bound for the estimation. These results demonstrate that the proposed features provide a strong retrospective mapping to the RUL labels within the completed degradation trajectory. They are not interpreted as prognostic for unseen cables' performance.

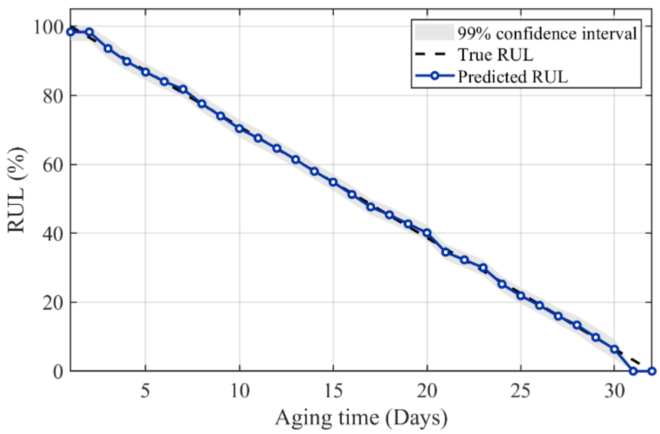

Figure 13. Retrospective within-trajectory RUL mapping with a 99% predictive interval using HI-assisted degradation features at 140 ℃.

The retrospective daily mapping results in Table 2 show that the proposed Riemannian-feature-based GPR model closely follows the true RUL trend over the full aging process. Most predicted values remain close to the corresponding true RUL values, and the 99% predictive intervals are relatively narrow, indicating stable prediction uncertainty. In the late aging stage, the predicted RUL rapidly approaches zero, which is consistent with the end-of-life condition.

Table 2. Retrospective daily RUL mapping results with 99% predictive intervals.

Day	True RUL (%)	Predicted RUL (%)	99% CI, lower (%)	99% CI, upper (%)
1	100.00	98.39	95.79	100.00
2	96.77	98.39	95.79	100.00
3	93.55	93.56	90.60	96.53
4	90.32	89.82	87.21	92.44
5	87.10	86.75	84.32	89.17
6	83.87	83.99	81.66	86.33
7	80.65	81.78	79.50	84.06
8	77.42	77.56	75.27	79.85
9	74.19	74.01	71.63	76.38
10	70.97	70.37	67.81	72.93
11	67.74	67.59	65.00	70.17
12	64.52	64.62	62.23	67.01
13	61.29	61.37	58.98	63.75
14	58.06	57.96	55.60	60.32
15	54.84	54.82	52.43	57.22
16	51.61	51.26	48.79	53.73
17	48.39	47.64	45.36	49.91
18	45.16	45.34	42.98	47.71
19	41.94	42.72	40.48	44.97
20	38.71	40.14	37.90	42.39

Continued on next page

Day	True RUL (%)	Predicted RUL (%)	99% CI, lower (%)	99% CI, upper (%)
21	35.48	34.52	32.23	36.80
22	32.26	32.29	30.01	34.58
23	29.03	30.02	27.74	32.31
24	25.81	25.26	22.96	27.56
25	22.58	21.88	19.58	24.19
26	19.35	19.08	16.73	21.44
27	16.13	15.97	13.58	18.36
28	12.90	13.39	10.74	16.04
29	9.68	9.81	6.90	12.72
30	6.45	6.36	3.54	9.19
31	3.23	0.00	0.00	0.11
32	0.00	0.00	0.00	0.00

The comparison in Table 3 is designed to evaluate whether the proposed HI-assisted Riemannian features provide more effective RUL information than conventional or single-feature inputs. The raw BIS baseline directly uses the original magnitude of impedance and phase spectra, followed by principal component analysis (PCA) for reducing dimensionality.

A LOOCV strategy is used for model evaluation. In each trial, one aging day is selected as the test sample, while the remaining days are used to train the GPR model. This process is repeated until every aging day has been tested once. Therefore, the reported RMSE, MAE, and R^2 values reflect the RUL mapping capability of each feature representation under the same training and testing strategy.

As shown in Table 3, raw BIS gives the weakest performance, confirming that direct spectral features are easily affected by resonance shifts and frequency misalignment. Compared with raw BIS, the proposed HI+E_{warp} method reduces the RMSE from 23.4370% to 0.9404% and the MAE from 15.5850% to 0.6768%, while increasing R^2 from 0.3808 to 0.9990. The single-feature models based on D_{shape} and E_{warp} improve the prediction accuracy, but each describes only one aspect of degradation: Residual geometric change or spectral warping. The HI-only model provides a more stable prediction by using monotonic cumulative degradation information. By further incorporating E_{warp}, the proposed model gains complementary frequency axis distortion information, leading to the best retrospective within-trajectory mapping performance. These results compare feature representations under an identical retrospective protocol and should not be interpreted as independent prediction performance for an unseen cable.

Table 3. Retrospective within-trajectory mapping performance using different feature inputs.

Feature input	RMSE (%)	MAE (%)	R^2
Raw BIS	23.4370	15.5850	0.3808
Only D_{shape}	12.1180	9.5568	0.8345
Only E_{warp}	8.4168	6.8966	0.9201
$D_{\text{shape}}+E_{\text{warp}}$	5.6381	3.5084	0.9642
HI	1.1219	0.7979	0.9986
Proposed (HI+E_{warp})	**0.9404**	**0.6768**	**0.9990**

5.4. Retrospective chronological tail-holdout validation

In addition to the retrospective day-wise LOOCV, a chronologically constrained tail-holdout experiment is conducted to examine temporally ordered extrapolation within the same completed 140 °C trajectory. Let t denote the last training day. Samples from Days 1 to t are used for model training, while Days $t + 1$ to $T_{\max}$ are used exclusively for testing. In this study, t is set to $T_{\max} - 1$, $T_{\max} - 2$, and $T_{\max} - 3$, corresponding to the prediction of the last one, two, and three days, respectively. The proposed feature vector consists of the training-referenced HI and E_{warp}, and no feature or target value from the held-out period is used during model fitting.

As shown in Figure 14 and Table 4, the proposed method achieved the best performance under all three prediction horizons. For the last two and three days, the proposed method obtains RMSE values of 0.434% and 0.450%, respectively, which are clearly lower than the 1.027% and 0.958% obtained using HI alone. For the one-day setting, RMSE and MAE are identical because only one test sample is included. Overall, the results demonstrate that the proposed fusion of monotonic HI and E_{warp} provides a more accurate and robust representation of late-stage degradation, leading to superior performance in terms of near-end-of-life RUL extrapolation.

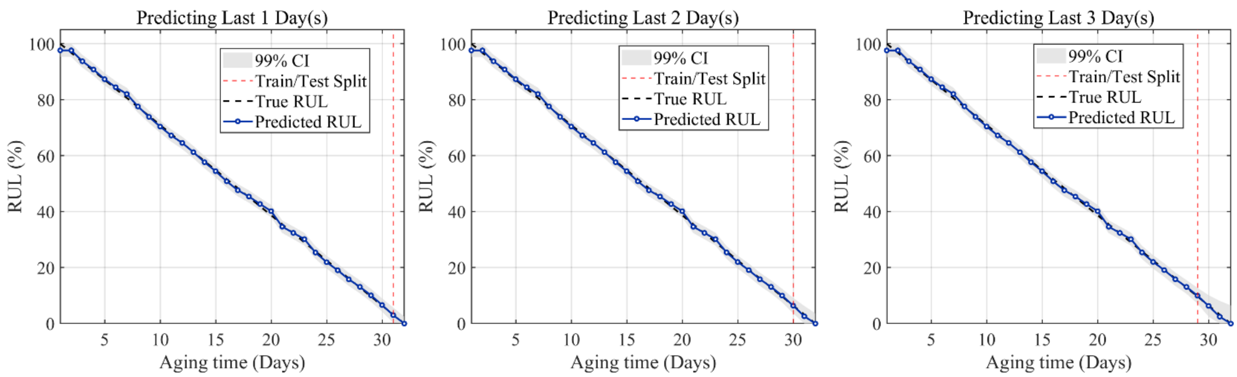

Figure 14. Retrospective chronological tail-holdout results for the final one, two, and three monitoring days.

Table 4. Retrospective within-trajectory extrapolation performance under chronological tail-holdout validation.

Feature input	Last 1 day	Last 2 days	Last 3 days
	RMSE/MAE (%)	RMSE/MAE (%)	RMSE/MAE (%)
Raw BIS	35.894/35.894	37.086/36.697	59.099/56.548
Only D_{shape}	14.894/14.894	14.374/14.205	14.551/14.262
Only E_{warp}	14.998/14.998	11.759 / 11.249	13.548/13.393
$D_{\text{shape}} + E_{\text{warp}}$	9.509/9.509	7.802/7.292	9.052/8.798
HI	1.637/1.637	1.027/0.906	0.958/0.945
Proposed (HI+ E_{warp})	**0.000/0.000**	**0.434/0.307**	**0.450/0.302**

5.5. Independent cross-temperature RUL prediction

To evaluate the prognostic performance without using any target information from the tested cables, the complete run-to-failure data obtained at 160 °C are used exclusively for GPR training, whereas the independently aged cables at 140 °C are used only for testing. The 1-m, 2-m, and 3-m cables are evaluated separately. For each tested cable, only the current $E_{\mathrm{warp}}(t)$ and the causally accumulated $G(t)$ are supplied to the trained model. The failure time, RUL labels, terminal CRSE value, and future BIS measurements of the 140 °C cables are not used during model training or prediction.

As shown in Table 5, the proposed $G + E_{\mathrm{warp}}$ feature representation achieves the best performance for all three cable lengths. For the 1-m, 2-m, and 3-m cables, RMSE values of 4.7237%, 5.5727%, and 1.8697% are obtained, respectively, while the corresponding R^2 values reach 0.9748, 0.9650, and 0.9960. The single G feature also provides relatively accurate predictions, whereas the additional E_{warp} feature further reduces the prediction error. In contrast, the raw BIS, D_{shape}, and E_{warp} alone show weaker cross-temperature generalization.

Table 5. Independent cross-temperature RUL prediction performance using different feature representations.

Feature input	1 m	2 m	3 m
	RMSE/MAE (%)/R^2	RMSE/MAE (%)/R^2	RMSE/MAE (%)/R^2
Raw BIS	50.9741/46.8838/−1.9290	49.4419/44.2975/−1.7556	42.8825/33.7235/−1.0729
Only D_{shape}	36.1178/32.3534/−0.4705	32.7264/23.2636/−0.2073	29.0355/22.3460/0.0496
Only E_{warp}	31.3196/26.6943/−0.1057	34.0214/26.6267/−0.3047	27.9440/22.4270/0.1197
$D_{\mathrm{shape}} + E_{\mathrm{warp}}$	13.9249/11.3293/0.7814	10.4087/4.7583/0.8778	9.9144/7.5032/0.8891
G	8.3599/6.3869/0.9212	6.0110/4.9186/0.9593	7.1470/6.1175/0.9424
Proposed ($G + E_{\mathrm{warp}}$)	**4.7237/4.2749/0.9748**	**5.5727/4.3456/0.9650**	**1.8697/1.4167/0.9960**

The predicted RUL trajectories in Figure 15 generally follow the true degradation trends for all cable lengths, and the associated 99% predictive intervals provide uncertainty bounds throughout the aging process. The errors are somewhat higher than those obtained in the retrospective within-trajectory analysis because the model is transferred between different aging temperatures and is evaluated on completely unseen cables' trajectories. Nevertheless, the consistently high R^2 values indicate that the proposed causal geometric features retain effective degradation information under independent cross-temperature testing.

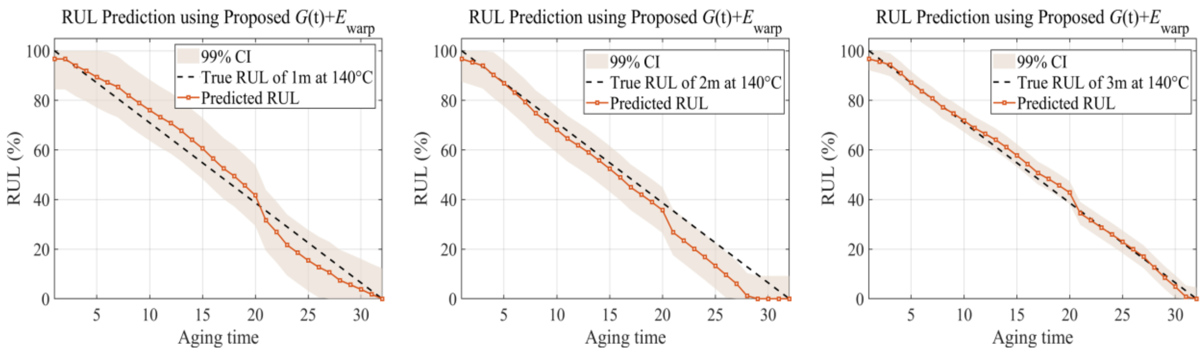

Figure 15. Independent cross-temperature RUL prediction results for the 1-m, 2-m, and 3-m cables at 140 °C using the GPR models trained exclusively on the 160 °C data.

5.6. Parameter sensitivity analysis

To retrospectively evaluate the numerical robustness of the proposed framework, sensitivity analyses are performed using the completed 32-day cable trajectory obtained at 140 °C. A one-factor-at-a-time strategy is adopted, in which one parameter is varied while the remaining settings are fixed at $L = 10$, $\varepsilon = 10^{-6}$, $\delta = 10^{-10}$, and the ARD squared exponential kernel. For each setting, construction of the complete SPD trajectory, LE-DTW alignment, HI generation, and GPR-based retrospective RUL prediction procedures are repeated using the same LOOCV strategy.

Sliding-window length. Table 6 shows that the proposed framework exhibits limited sensitivity to the sliding-window length within the tested range. The RMSE ranges from 0.9404% to 1.1798%, the MAE ranges from 0.6768% to 0.7716%, and all R^2 values remain above 0.9987. The best overall performance is obtained at $L = 10$. An excessively short window may reduce the covariance stability of the estimation, whereas an excessively long window may partially smooth localized spectral variations. Therefore, $L = 10$ is selected as a balanced setting between local spectral resolution and covariance stability.

Table 6. Retrospective sensitivity analysis of L for RUL prediction at 140 °C.

L	RMSE (%)	MAE (%)	R^2
5	0.9960	0.6876	0.9989
8	0.9425	0.6841	**0.9990**
10	**0.9404**	**0.6768**	**0.9990**
15	1.0512	0.7404	0.9988
20	1.1798	0.7716	0.9987

SPD covariance regularization coefficient. Table 7 shows that the retrospective mapping performance remains relatively stable when ε ranges from 10^{-5} to 10^{-8}. Although $\varepsilon = 10^{-7}$ yields the lowest RMSE, $\varepsilon = 10^{-6}$ produces the lowest MAE, and both settings achieve $R^2 = 0.9990$. In contrast, $\varepsilon = 10^{-4}$ results in larger prediction errors, indicating that excessive regularization may alter the local covariance structure. Therefore, $\varepsilon = 10^{-6}$ is retained as a balanced setting.

Table 7. Retrospective sensitivity analysis of ε for RUL prediction at 140 °C.

ε	RMSE (%)	MAE (%)	R^2
10^{-4}	1.3373	0.8886	0.9980
10^{-5}	1.0241	0.7089	0.9988
$\mathbf{10^{-6}}$	0.9404	**0.6768**	**0.9990**
10^{-7}	**0.9362**	0.6810	**0.9990**
10^{-8}	0.9485	0.6873	**0.9990**

SRVF zero-velocity threshold. As shown in Table 8, the retrospective mapping performance remains highly stable across the tested values of δ. For $\delta \leq 10^{-8}$, the results remain unchanged because these thresholds are below the minimum nonzero log-domain velocity norm, which is approximately 10^{-7}. Larger thresholds cause only marginal changes in RMSE and MAE, while R^2 remains approximately 0.9990. These results indicate that δ primarily serves as a numerical safeguard. Therefore, $\delta = 10^{-10}$ is retained to prevent numerical singularity without suppressing valid trajectory variations.

Table 8. Retrospective sensitivity analysis of δ for RUL prediction at 140 °C.

δ	RMSE (%)	MAE (%)	R^2
10^{-3}	0.9433	0.6799	0.9990
10^{-4}	0.9408	0.6769	0.9990
10^{-6}	0.9424	0.6793	0.9990
10^{-8}	0.9404	0.6768	0.9990
$\mathbf{10^{-10}}$	**0.9404**	**0.6768**	**0.9990**
10^{-12}	0.9404	0.6768	0.9990

GPR kernel function. Table 9 shows that the RUL-related retrospective mapping performance remains stable across the tested GPR kernel functions. The RMSE ranges from 0.9404% to 1.0506%, and all R^2 values exceed 0.9989. Among the tested kernels, the Matérn kernel is a stationary covariance function whose smoothness is controlled by the parameter v, with v=3/2 and v=5/2 corresponding to the automatic relevance determination (ARD) Matérn 3/2 and ARD Matérn 5/2 kernels considered here, respectively. The ARD squared exponential kernel achieves the lowest RMSE and MAE and is therefore adopted in the proposed framework. For each kernel, the length scales, signal variance, and noise variance are automatically estimated from the training data within each cross-validation fold rather than manually fixed.

Overall, the results demonstrate that the proposed framework is robust to moderate variations in the main numerical and modeling parameters.

Table 9. Retrospective sensitivity analysis of different GPR kernel functions for RUL prediction at 140 °C.

GPR kernel function	RMSE (%)	MAE (%)	R^2
ARD squared exponential	**0.9404**	**0.6768**	**0.9990**
ARD exponential	1.0506	0.7034	0.9989
ARD Matérn 3/2	1.0132	0.6988	0.9989
ARD Matérn 5/2	0.9749	0.6863	0.9990
ARD rational quadratic	0.9693	0.6915	0.9990

6. Conclusions

This paper proposed a Riemannian manifold-valued trajectory modeling and elastic alignment framework for cable degradation analysis. The measured cable responses were first converted into localized SPD covariance matrices through a sliding-window strategy, so that each cable state was represented as a continuous trajectory on the SPD manifold. By introducing log-Euclidean coordinates and SRVF representation, the proposed framework converted the comparison of broadband cable responses into an elastic alignment problem of manifold-valued trajectories.

These trajectories were then aligned using LE-DTW to estimate the optimal monotone correspondence. The optimized warping path characterized horizontal frequency axis distortion, while the residual shape distance quantified the residual log-Euclidean geometric variation remaining after alignment. In this way, the proposed method separated parameter axis misalignment from degradation-related trajectory deformation, avoiding the limitations of fixed-frequency indicators and direct Euclidean comparison.

The effectiveness of the framework was verified using cable degradation data under different cable lengths, thermal stresses, and spatial aging locations. The results showed that length-, temperature-, and location-induced spectral distortions were mainly absorbed by the warping path, whereas the residual shape distance preserved degradation-related geometric information. Furthermore, CRSE was constructed from the residual shape distance and normalized into a monotonic HI. The HI and warping energy were further fused and used in GPR for retrospective degradation analysis. Compared with raw measurement features, the proposed method reduced RMSE from 23.4370% to 0.9404% and MAE from 15.5850% to 0.6768%, while increasing R^2 from 0.3808 to 0.9990. For independent RUL prediction, the causal cumulative feature was fused with the warping energy and used in GPR. Under the independent cross-temperature protocol, the proposed method achieved RMSE values of 4.7237%, 5.5727%, and 1.8697% for the 1-m, 2-m, and 3-m cables, respectively, with corresponding R^2 values of 0.9748, 0.9650, and 0.9960. Together, the two experiments demonstrated both the degradation-representation capability and the independent prognostic value of the proposed features.

Overall, the study demonstrated that cable degradation could be effectively described as a non-Euclidean manifold-valued trajectory evolution problem. The proposed Riemannian elastic alignment framework provided a mathematically interpretable way to model ordered multichannel responses with nonlinear parameter distortion.

One limitation of the present framework is that the SRVF representation and dynamic programming alignment are implemented in the flat symmetric-matrix space induced by the log-Euclidean metric. Therefore, the nonzero curvature of the SPD manifold is not explicitly incorporated into the alignment procedure. Future work will investigate a more intrinsic elastic analysis of SPD-valued trajectories by constructing SRVF representations directly on homogeneous spaces [40]. This extension may better preserve the curved manifold geometry while enabling further evaluation of the trade-off among geometric fidelity, numerical stability, and computational complexity.

Author contributions

Zigang Liu: Conceptualization, methodology, software, validation, formal analysis, investigation, data curation, writing – original draft preparation and visualization; Tianyao Ji: Conceptualization, validation, resources, writing – review and editing, supervision, project administration, and funding acquisition; Zeineb Klai: Methodology, investigation, resources, writing – review and editing, supervision, project administration and funding acquisition; Saleh M. Altowaijri: Resources, writing – review and editing, project administration. All authors have read and approved the final version of the manuscript for publication.

Use of generative AI tools declaration

The authors declare they have not used Artificial Intelligence (AI) tools in the creation of this article.

Acknowledgments

The authors extend their appreciation to the Deanship of Scientific Research at Northern Border University, Arar, Kingdom of Saudi Arabia, for funding this research work through the project number NBU-FPEJ-2026-2942-02. The authors also would like to thank Rheinisch-Westfälische Technische Hochschule (RWTH) Aachen University, Germany, for providing the experimental data used in this study.

Conflict of interest

All authors declare no conflicts of interest in this paper.

References

1. X. Wang, M. N. Al Imran, M. Ali, B. Zhang, Interdigital capacitor sensor-based cable health monitoring, *IEEE T. Ind. Electron.*, **70** (2023), 7301–7309. https://doi.org/10.1109/TIE.2022.3203764
2. Z. Lin, H. Chen, Q. Wu, T. Ji, Extreme scenarios based data-adaptive probability uncertainty set for distributionally robust transmission expansion planning, *CSEE J. Power Energy*, **10** (2024), 2675–2679. https://doi.org/10.17775/CSEEJPES.2021.01860
3. J. Zhu, B. Chen, T. Ji, Z. Jing, Transitional revenue scheme for high-cost generator unit in Guangdong electricity market based on government authorized contracts, *CSEE J. Power Energy*, **10** (2024), 208–221. https://doi.org/10.17775/CSEEJPES.2020.03040

4. B. Deng, X. Xu, M. Li, T. Ji, Q. H. Wu, Two-stage multi-objective optimization and decision-making method for integrated energy system under wind generation disturbances, *CSEE J. Power Energy*, **10** (2024), 2564–2576. https://doi.org/10.17775/CSEEJPES.2023.07130
5. A. van Deursen, P. Wouters, F. Steenis, Corrosion in low-voltage distribution networks and perspectives for online condition monitoring, *IEEE T. Power Deliver.*, **34** (2019), 1423–1431. https://doi.org/10.1109/TPWRD.2019.2903730
6. G. C. Montanari, D. Fabiani, P. Morshuis, L. Dissado, Why residual life estimation and maintenance strategies for electrical insulation systems have to rely upon condition monitoring, *IEEE T. Dielect. El. In.*, **23** (2016), 1375–1385. https://doi.org/10.1109/TDEI.2015.005613
7. J. C. Fothergill, S. J. Dodd, L. A. Dissado, T. Liu, U. H. Nilsson, The measurement of very low conductivity and dielectric loss in XLPE cables: A possible method to detect degradation due to thermal aging, *IEEE T. Dielect. El. In.*, **18** (2011), 1544–1553. https://doi.org/10.1109/TDEI.2011.6032823
8. J. Hernandez-Mejia, R. Harley, N. Hampton, R. Hartlein, Characterization of ageing for MV power cables using low frequency tan δ diagnostic measurements, *IEEE T. Dielect. El. In.*, **16** (2009), 862–870. https://doi.org/10.1109/TDEI.2009.5128527
9. H. A. Illias, M. A. Tunio, A. H. A. Bakar, H. Mokhlis, G. Chen, Partial discharge phenomena within an artificial void in cable insulation geometry: Experimental validation and simulation, *IEEE T. Dielect. El. In.*, **23** (2016), 451–459. https://doi.org/10.1109/TDEI.2015.005155
10. C. Furse, Y. C. Chung, R. Dangol, M. Nielsen, G. Mabey, R. Woodward, Frequency-domain reflectometry for on-board testing of aging aircraft wiring, *IEEE T. Electromagn. C.*, **45** (2003), 306–315. https://doi.org/10.1109/TEMC.2003.811305
11. C. Buccella, M. Feliziani, G. Manzi, Detection and localization of defects in shielded cables by time-domain measurements with UWB pulse injection and clean algorithm postprocessing, *IEEE T. Electromagn. C.*, **46** (2004), 597–605. https://doi.org/10.1109/TEMC.2004.837842
12. X. Dai, J. Hao, Z. Jian, K. H. Al Hosani, R. Liao, Insights into nonuniform aging effects on broadband dielectric behaviors for high-voltage XLPE cable insulation: A novel fractional-order circuit modeling approach, *IEEE T. Dielect. El. In.*, **32** (2025), 1793–1801. https://doi.org/10.1109/TDEI.2024.3466127
13. Z. Zhou, D. Zhang, J. He, M. Li, Local degradation diagnosis for cable insulation based on broadband impedance spectroscopy, *IEEE T. Dielect. El. In.*, **22** (2015), 2097–2107. https://doi.org/10.1109/TDEI.2015.004799
14. G. Frusque, I. Nejjar, M. Nabavi, O. Fink, Semisupervised health index monitoring with feature generation and fusion, *IEEE T. Reliab.*, **74** (2025), 4005–4019. https://doi.org/10.1109/TR.2024.3496076
15. H. Liu, Z. Liu, D. Zhang, W. Jia, X. Xin, J. Tan, Uncertainty quantification and interval prediction of equipment remaining useful life based on semisupervised learning, *IEEE Trans. Instrum. Meas.*, **73** (2023), 3506315. https://doi.org/10.1109/TIM.2023.3334339
16. W. Cao, Z. Meng, J. Li, J. Wu, F. Fan, A remaining useful life prediction method for rolling bearing based on TCN-Transformer, *IEEE T. Instrum. Meas.*, **74** (2024), 3501309. https://doi.org/10.1109/TIM.2024.3502878

17. S. Iglesias-Perez, A. Partida, R. Criado, The advantages of k-visibility: A comparative analysis of several time series clustering algorithms, *AIMS Mathematics*, **9** (2024), 35551–35569. https://doi.org/10.3934/math.20241687
18. H. Sakoe, S. Chiba, Dynamic programming algorithm optimization for spoken word recognition, *IEEE T. Acoust Speech Signal Process.*, **26** (1978), 43–49. https://doi.org/10.1109/TASSP.1978.1163055
19. T. Ji, Z. Liu, X. Zhuang, Q. Li, L. Zhang, Q. H. Wu, Advancing GIS operational monitoring: A novel voiceprint recognition method using Grassmann manifold and multi-kernel functions, *IEEE T. Power Deliver.*, **39** (2024), 2894–2907. https://doi.org/10.1109/TPWRD.2024.3448354
20. C. Ju, C. Guan, Graph neural networks on SPD manifolds for motor imagery classification: A perspective from the time–frequency analysis, *IEEE T. Neur. Net. Lear.*, **35** (2024), 17701-17715. https://doi.org/10.1109/TNNLS.2023.3307470
21. R. Wang, X. J. Wu, Z. Chen, C. Hu, J. Kittler, SPD manifold deep metric learning for image set classification, *IEEE T. Neur. Net. Lear.*, **35** (2024), 8924–8938. https://doi.org/10.1109/TNNLS.2022.3216811
22. G. L. W. Vom Berg, V. Röhr, D. Platt, B. Blankertz, A new canonical Log-Euclidean kernel for symmetric positive definite matrices for EEG analysis (Oct 2024), *IEEE T. Biomed. Eng.*, **72** (2025), 1000–1007. https://doi.org/10.1109/TBME.2024.3483936
23. Z. Liu, F. F. M. El-Sousy, N. Ali Larik, H. Quan, T. Ji, Riemannian geodesic discriminant analysis–minimum Riemannian mean distance: A robust and effective method leveraging a symmetric positive definite manifold and discriminant algorithm for image set classification, *Mathematics*, **12** (2024), 2164. https://doi.org/10.3390/math12142164
24. Z. Liu, Y. Wu, H. Quan, T. Ji, A non-Euclidean method for open-circuit fault diagnosis in back-to-back converters leveraging SPD manifold and mathematical morphological filtering, *IEEE T. Power Electr.*, **41** (2026), 11268–11283. https://doi.org/10.1109/TPEL.2026.3658883
25. M. Sutti, M. H. Yueh, Riemannian gradient descent for spherical area-preserving mappings, *AIMS Mathematics*, **9** (2024), 19414–19445. https://doi.org/10.3934/math.2024946
26. I. Chami, Z. Ying, C. Ré, J. Leskovec, Hyperbolic graph convolutional neural networks, *Adv. Neural Inf. Process. Syst.*, **32** (2019), 4869–4880.
27. L. Sun, Z. Huang, Q. Wan, H. Peng, P. S. Yu, Spiking graph neural network on Riemannian manifolds, In: *38th Conference on Neural Information Processing Systems (NeurIPS 2024)*, **37** (2024), 34025–34055. https://doi.org/10.52202/079017-1071
28. L. Sun, Z. Huang, S. Zhou, Q. Wan, H. Peng, P. S. Yu, RiemannGFM: Learning a graph foundation model from Riemannian geometry, In: *WWW '25: Proceedings of the ACM on Web Conference 2025*, 2025, 1154–1165. https://doi.org/10.1145/3696410.3714952
29. L. Li, Z. Jin, X. Zhang, H. Duan, J. Wang, Z. Tao, H. Zhao, X. Zhu, Multi-view Riemannian manifolds fusion enhancement for knowledge graph completion, *IEEE T. Knowl. Data En.*, **37** (2025), 2756–2770. https://doi.org/10.1109/TKDE.2025.3538110
30. L. Sun, Q. Wan, S. Zhou, Z. Huang, P. S. Yu, RiemannGL: Riemannian geometry changes graph deep learning, 2026, arXiv:2602.10982. https://doi.org/10.48550/arXiv.2602.10982
31. A. Srivastava, E. Klassen, S. H. Joshi, I. H. Jermyn, Shape analysis of elastic curves in Euclidean spaces, *IEEE T. Pattern Anal.*, **33** (2011), 1415–1428. https://doi.org/10.1109/TPAMI.2010.184

32. M. Bruveris, Optimal reparametrizations in the square root velocity framework, *SIAM J. Math. Anal.*, **48** (2016), 4335–4354. https://doi.org/10.1137/15M1014693
33. J. D. Tucker, W. Wu, A. Srivastava, Generative models for functional data using phase and amplitude separation, *Comput. Stat. Data An.*, **61** (2013), 50–66. https://doi.org/10.1016/j.csda.2012.12.001
34. E. Hartman, Y. Sukurdeep, E. Klassen, N. Charon, M. Bauer, Elastic shape analysis of surfaces with second-order Sobolev metrics: A comprehensive numerical framework, *Int. J. Comput. Vis.*, **131** (2023), 1183–1209. https://doi.org/10.1007/s11263-022-01743-0
35. S. Jeong, W. Ko, A. W. Mulyadi, H.-I. Suk, Deep efficient continuous manifold learning for time series modeling, *IEEE T. Pattern Anal.*, **46** (2024), 171–184. https://doi.org/10.1109/TPAMI.2023.3320125
36. G. Wang, H. Laga, A. Srivastava, Elastic shape analysis of tree-like 3D objects using extended SRVF representation, *IEEE T. Pattern Anal.*, **46** (2024), 2475–2488. https://doi.org/10.1109/TPAMI.2023.3334525
37. J. Richter, C. A. Erdős, C. Scheurer, J. J. Steil, N. Dehio, Riemannian time warping: Multiple sequence alignment in curved spaces, *IEEE Robot. Autom. Let.*, **10** (2025), 10894–10901. https://doi.org/10.1109/LRA.2025.3604734
38. Y. S. Zhao, P. Li, Y. Kang, Y. B. Zhao, A health indicator enabling both first predicting time detection and remaining useful life prediction: Application to rotating machinery, *Measurement*, **235** (2024), 114994. https://doi.org/10.1016/j.measurement.2024.114994
39. B. M. Agua, S. Bouzebda, Single index regression for locally stationary functional time series, *AIMS Mathematics*, **9** (2024), 36202–36258. https://doi.org/10.3934/math.20241719
40. Z. Su, E. Klassen, M. Bauer, Comparing curves in homogeneous spaces, *Differ. Geom. Appl.*, **60** (2018), 9–32. https://doi.org/10.1016/j.difgeo.2018.05.001

Appendix

Table A1. Key numerical implementation settings.

Parameter	Meaning	Value
L	Sliding-window length	10
ε	SPD covariance regularization coefficient	10^{-6}
δ	SRVF zero-velocity threshold	10^{-10}
λ	Warping regularization coefficient	0
K	Number of frequency points	1000
W	Number of localized sliding windows	991
N	Number of SRVF segments	990
Kernel	GPR kernel function	ARD squared exponential